metals

MDPI

Review

The Potential of Duplex Stainless Steel Processed by Laser Powder Bed Fusion for Biomedical Applications: A Review

Maria Laura Gatto [1,*,†], Alberto Santoni [1,†], Eleonora Santecchia [1], Stefano Spigarelli [1], Fabrizio Fiori [2], Paolo Mengucci [3] and Marcello Cabibbo [1]

[1] Department of Industrial Engineering and Mathematical Sciences, Polytechnic University of Marche, Via Brecce Bianche, 60131 Ancona, Italy; a.santoni@pm.univpm.it (A.S.); e.santecchia@univpm.it (E.S.); s.spigarelli@univpm.it (S.S.); m.cabibbo@univpm.it (M.C.)
[2] Department DISCO, Università Politecnica delle Marche, Via Brecce Bianche 12, 60131 Ancona, Italy
[3] Department SIMAU & UdR INSTM, Università Politecnica delle Marche, Via Brecce Bianche 12, 60131 Ancona, Italy
* Correspondence: m.l.gatto@univpm.it
† These authors contributed equally to this work.

Abstract: The austenitic stainless steels utilized in the production of osteosynthesis devices are susceptible to crevice corrosion. Several studies have compared the corrosive behavior of austenitic and duplex stainless steels (DSS), both of which are recognized as viable biomaterials for tissue engineering applications. All of the in vitro and in vivo studies on animals and clinical results reported to date indicate that austeno-ferritic duplex stainless steel can be recommended as a suitable alternative to ASTM F138 steel, since it is resistant to crevice corrosion in the human body and presents superior mechanical properties. The use of DSS for biomedical applications is still under discussion, mainly due to the lack of knowledge of its behavior in terms of device heating or induced movement when exposed to magnetic fields, a potentially harmful effect for the human body. As a breakthrough production technology, additive manufacturing (AM) has demonstrated significant benefits for the fabrication of metal devices with patient-specific geometry. Laser powder bed fusion has particularly been used to manufacture DSS-based components. A fine control of the processing conditions allows for an understanding of DSS microstructural evolution, which is essential for selecting processing parameters and estimating performance, including mechanical properties and corrosion resistance. Furthermore, scientific investigation is necessary for determining the relationships among material, process, and magnetic properties, in order to establish the underlying principles and critical responses. The purpose of this review is to highlight the key performances of DSS for biomedical applications and to point out the relevant role of advanced processing technologies such as additive manufacturing.

Keywords: duplex stainless steel; laser powder bed fusion; microstructure; mechanical properties; corrosion resistance; magnetic behavior; biomedical applications

check for updates

Citation: Gatto, M.L.; Santoni, A.; Santecchia, E.; Spigarelli, S.; Fiori, F.; Mengucci, P.; Cabibbo, M. The Potential of Duplex Stainless Steel Processed by Laser Powder Bed Fusion for Biomedical Applications: A Review. *Metals* **2023**, *13*, 949. https://doi.org/10.3390/met13050949

Academic Editors: Mădălina Simona Bălțatu and Petrică Vizureanu

Received: 24 March 2023
Revised: 30 April 2023
Accepted: 11 May 2023
Published: 14 May 2023

Copyright: © 2023 by the authors. Licensee MDPI, Basel, Switzerland. This article is an open access article distributed under the terms and conditions of the Creative Commons Attribution (CC BY) license (https://creativecommons.org/licenses/by/4.0/).

1. Introduction

Among the traditional biomaterials for grafting, cobalt-chromium and titanium alloys are used for permanent implants [1], while stainless steel alloys are generally employed for temporary ones. Additionally, when a second surgery to remove the temporary implant after tissue healing leads to increased patient morbidity and healthcare costs, biomaterials that biocorrode, such as magnesium alloys [2] and Fe-Mn alloys [3], are currently attracting significant interest. As a temporary non-degradable implant, austenitic stainless steels (ASTM F138/139 and ASTM F745) are commonly used in the production of load bearing components promoting bone healing, such as bone plates and nails for the shinbone, screws, pins, sutures, and steel threads and networks used in fixing fractures [4]. Specifically, ASTM F138/139 is employed for device fabrication by forging and machining

processes, whereas ASTM F745 is utilized for cast implants. In addition to their inexpensive cost, these materials are biocompatible and possess adequate mechanical, physical and electrochemical properties. Nevertheless, the austenitic stainless steels (SS) show low corrosion resistance when exposed to body fluids. Consequently, prolonged contact with these chloride-ion-containing aggressive media may increase the likelihood of localized corrosion [5]. The eventual corrosion, in addition to causing the chemical and mechanical degradation of the implant, promotes the release of metallic ions into the surrounding tissues, which, as the case of nickel (Ni), can cause metal allergy, carcinogenicity, cytotoxicity, and genotoxicity when released in concentrations that exceed the admissible levels [5]. Moreover, austenitic SS have insufficient fatigue resistance for several extremely high stressed orthopedic devices, such as Harrington rods for the treatment of scoliosis and sliding-compression plate-screw systems [6]. Consequently, several research studies have focused on providing an alternative to the traditional austenitic SS employed in the biomedical field, focusing on duplex stainless steels in order to preserve the advantages of austenitic SS, while overcoming their application limits. Duplex stainless steels (DSS) show a peculiar double phase structure that contains approximately equal amounts of the ferrite and austenite phases (Figure 1), resulting in a useful combination of mechanical properties and corrosion resistance [7].

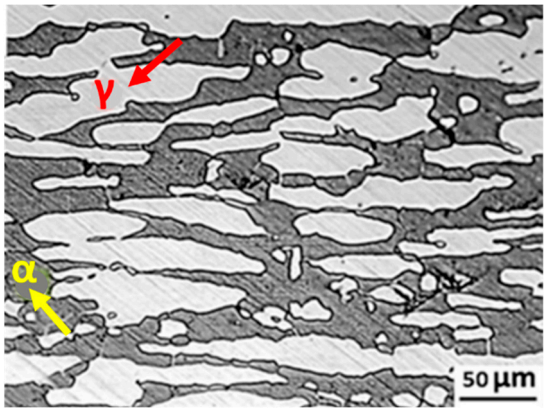


Figure 1. Typical microstructure of a duplex stainless steel (DSS 2205)—Red arrow indicates the ferritic phase, while yellow arrow indicates the austenitic phase. Figure adapted with permission from Ref. [8]. Copyright (2022), Elsevier.

The properties of duplex stainless steels are primarily determined by their chemical composition and thermal history. C, Cr, Ni, Mn, N and Mo are the most major alloying elements in DSS, but small amounts of Cu, W and rare earth elements are also present [9]. Alloying elements can be divided into ferrite stabilizing elements (such as Cr, Mo, and Si) and austenite stabilizing elements, such as Ni and N [4,10]. The Schaeffler diagram in Figure 2A illustrates their effect on the final phase configuration: a proper Cr_{eq} and Ni_{eq} content (wt%), which determines the stability of the two-phase ratio.

The formation of carbides, precipitates and secondary phases is likely to take place during heat treatments (Figure 2B) because of the thermal instability of the microstructure. Since their formation considerably affects both mechanical properties and corrosion resistance, a critical balance between the two-phase ratio and the avoidance of harmful precipitates formation must be ensured [8,11,12]. As an example, the brittle tetragonal σ–phase, which forms due to the increased amount of ferrite stabilizing elements, leads to a remarkable ductility degradation and increased corrosion susceptibility, which can be observed even with a small portion of this phase [13,14].

The presence of the ferrite phase increases the stress corrosion cracking and the yield strength of austenitic stainless steels, while the presence of the austenite phase may increase the toughness of ferritic stainless steel. Moreover, the ferritic phase of DSS exhibits excellent magnetic properties, confirming its application in endoprostheses gadget-like

magnetic stent materials [1,15]. However, the effects of the eventual exposure to magnetic fields should be thoroughly investigated in order to prevent potential harm to the human body [1,15]. The reduced nickel content of DSS, as compared to austenitic stainless steel, allows for the eliminating or minimizing of the adverse effects of the allergic reaction caused by Ni release. Therefore, DSS are considered as alternative materials to austenitic stainless steel for use in the medical industry [16,17]. The popularity of DSS has spurred the producers to create further duplex stainless steels containing varying amounts of alloying elements. Standard duplex, lean duplex, hyper duplex, and super duplex are some of the DSS, and are categorized according to their pitting resistance equivalent number values [7]. Therefore, the behavior of several DSS alloys has been studied in the literature by in vitro and in vivo tests, with the aim of overcoming traditional stainless steel issues in biomedical applications. In vitro tests found in the literature on DSS mostly investigated material corrosion behavior and mechanical properties. Several studies also focused on the improvement of surface corrosion resistance following surface treatment and coating, as well as on the magnetic properties of DSS. No studies on cell response to DSS have been reported in the literature as of yet, whereas in vivo biological tests aiming to understand the DSS behavior in contact with biological tissues have been conducted on small animals.

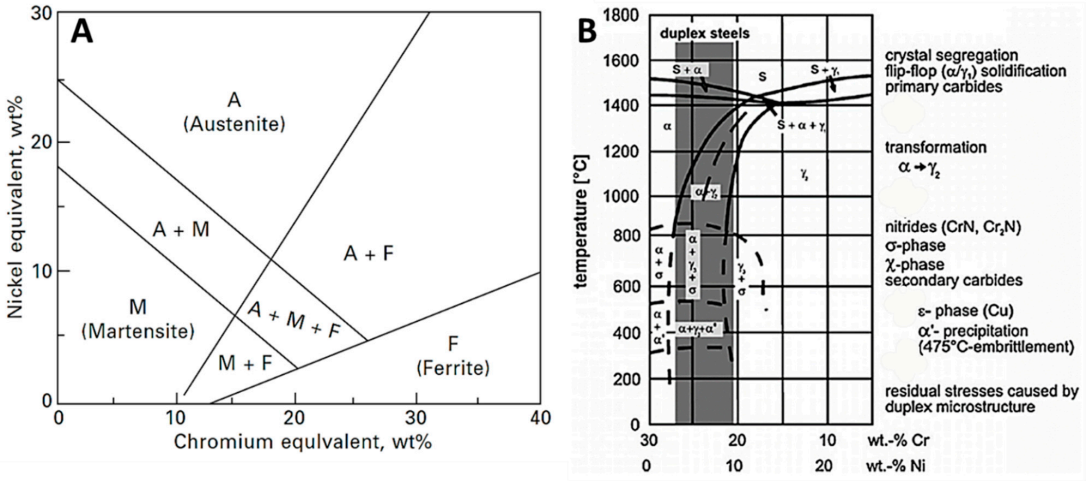


Figure 2. Phase configuration of DSS: (**A**) Schaeffler diagram—Nickel equivalent = Ni + Co + 30C + 25N + 0.5Mn + 0.3Cu; Chromium equivalent = Cr + 2Si + 1.5Mo + 5V + 5.5Al + 1.75Nb + 1.5Ti + 0.75W; and (**B**) Pseudo-binary Fe-Cr-Ni phase diagram at 70% Fe. Figures adapted with permission from Ref. [8]. Copyright (2022), Elsevier.

It is worth noting that research on DSS as a biomaterial has proceeded in parallel with the general increase in interest in DSS over the past 40 years (Figure 3). Scientific publications from the Scopus database were used in this study to retrieve the trend of article publication illustrated in Figure 3, based on the following keywords: "Duplex Stainless Steel" (Figure 3A) and "Duplex Stainless Steel" and "Biomaterial" (Figure 3B).

In recent years, research on DSS produced by additive manufacturing (AM) techniques has rapidly grown, as is visible from the trend of article publication from the Scopus database based on the keywords "Duplex Stainless Steel" and "Additive Manufacturing", as shown in Figure 4.

However, to the best of the authors' knowledge, no study has focused on combining DSS and AM technologies for biomedical applications.

Additive manufacturing (AM) is an advanced technique used to build complex structures by adding material layer-by-layer using 3D model data. AM has shown a great potential in the biomedical field, due to advantages such as the production of customized biomedical products, cost effectiveness, improved productivity, accessibility, and short production time [18]. In an increasing number of case studies, traditional manufacturing techniques are no longer competitive with this advancing technology for the production of

one-of-a-kind end-use medical devices [19]. Powder bed fusion (PBF) is one of the most widely used AM methods. In the PBF process, a heat source (laser or electron beam) is focused over a powder material layered on a bed, and melts the intended cross-sectional area according to the component design [20,21]. The laser powder bed fusion (L-PBF) technology, in particular, is highly suitable for biomedical applications such as pre-surgical planning, prosthetics, and bone scaffolds for tissue engineering [22], given the high level of detail and the accuracy typical of this laser-based AM technology. L-PBF technology can effectively control the pore size, distribution, and porosity level of porous bone implants, allowing patient customization [23]. Stainless steel was among the first metals to be used in L-PBF processes, and today several biocompatible stainless steel alloys fabricated by L-PBF, such as 304 or 316 L, are readily available on the market [23,24]. Laser re-melting during the L-PBF process allowed for the achievement of a relative density of stainless steel devices of over 99.9%. Additionally, the rapid cooling during the L-PBF process results in a refined stainless steel microstructure, enhancing the tensile strength with a reduction in ductility. A fine cellular dendritic structure is characteristic of 316L parts produced by L-PBF due to the rapid solidification during the process. This results in the higher strength obtained as compared to forged 316 L stainless steel parts, which experience lower cooling rates. Furthermore, a surface roughness of about 20 µm can be achieved via L-PBF, enabling implant osteointegration. Laser re-melting or post processing, such as sand-blasting, shot-peening, or manual grinding can be used to achieve a smooth and shiny surface [25]. In this review work, the performances of duplex stainless steel manufactured by L-PBF are reviewed, assuming as a reference the behavior of 316L stainless steel, which is widely studied in the literature as a result of its biomedical applications.

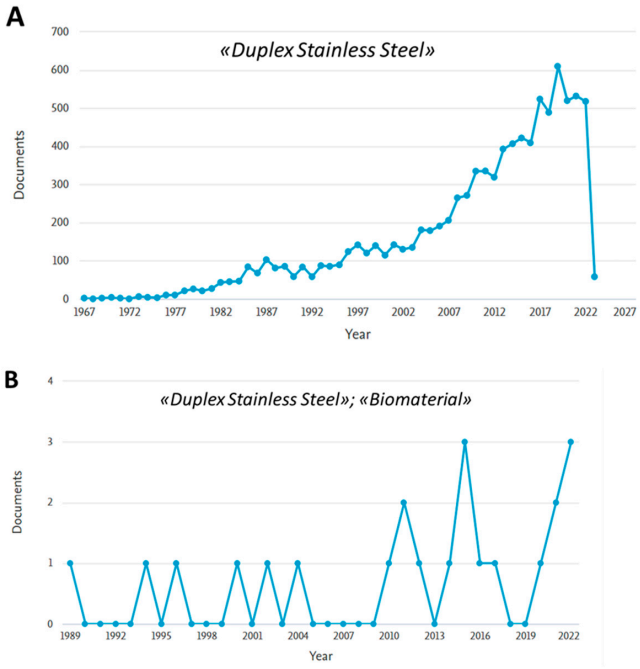


Figure 3. Diagram of the trend of article publication from the Scopus database, based on the keywords: (**A**) "Duplex Stainless Steel"; (**B**) "Duplex Stainless Steel", and "Biomaterial".

However, given all the phenomena involved in the L-PBF production process (i.e., laser-powder interaction drawbacks and very high solidification rates), the fabrication of devices with a high surface quality and a fixed and predictable microstructure is still quite challenging. A fine control of the AM process and post-processing conditions would allow for an understanding of the microstructural evolution of DSS, which is a critical point for designing the performance of biomedical devices, including mechanical properties and corrosion resistance [8]. In addition, establishing a material-process-magnetic-response

relationship would permit for the controlling of critical magnetic behaviour during the in vivo use of the device [26].

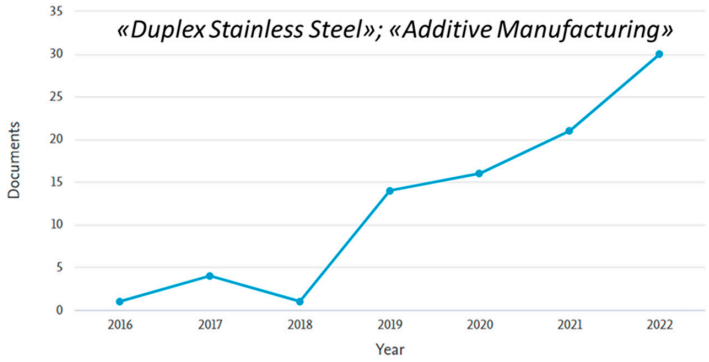


Figure 4. Diagram of the trend of article publication from the Scopus database based on the keywords "Duplex Stainless Steel" and "Additive Manufacturing".

The purpose of this review is to highlight the key performance of DSS for biomedical applications and to point out the relevant role of advanced processing technologies in additive manufacturing in order to stimulate a scientific interest in combining DSS and L-PBF technology for biomedical applications.

2. DSS for Biomedical Applications

2.1. In Vitro Performances

Complex service conditions are determined by two major conditions that lead to biomaterial failure [27]:

(1) The human body fluids comprising minerals, ionic salts, hydrolytic enzymes, proteins, nucleic acids, gases, carbonates, and lipids, thus representing an extremely tough environment;
(2) The demanding loading conditions.

In vitro tests on DSS found in the literature mostly investigated the material corrosion behavior and mechanical properties, as summarized in Table 1. Several studies also focused on the improvement of surface corrosive behavior following surface treatment and coating and on the magnetic properties of DSS (Table 1). In most studies, the performance of duplex steels is compared with the austenitic ones, which are most commonly used in the medical field (Table 1).

2.1.1. Corrosion Behavior

According to the findings of Cigada et al. [28], 25Cr-7Ni-4Mo-0.28N DSS (SAF 2507) exhibits the highest localized corrosion resistance among the investigated austenitic SS (AISI 316L, ASTM F138 and 27Cr-31Ni-3.5Mo) and traditional DSS (23Cr-4Ni and 22Cr-5Ni-3Mo (SAF 2205)), allowing it to be deemed not susceptible to crevice corrosion in the human body [28]. Specifically, the ranking of localized corrosion resistance in artificial physiological solution of the tested steels is as follows: 23Cr-4Ni < AISI 316L < ASTM F138 < 22Cr-5Ni-3Mo (SAF 2205) < 27Cr-31Ni-3.5Mo < 25Cr-7Ni-4Mo-N (SAF 2507) [2,29].

Despite the fact that SAF 2507 is renowned for its excellent mechanical strength and exceptional corrosion resistance, especially in chloride-rich environments, duplex stainless steels have not yet been accepted as implant materials due to the ferrimagnetic properties of the ferritic phase [30].

The corrosive behaviour of 2507 and 2205 DSS was also compared by Hammood et al. [17] in artificial saliva for orthodontic wire applications. SAF 2507 shows a higher corrosion resistance in artificial saliva than SAF 2205 before and after heat treatment, which is required in order to break down or dissolve secondary phases (sigma phase), remove segregation and to relieve any residual thermal stresses of the production process [17].

Electrochemically, cast 25Cr-7Ni-4Mo-N DSS outperforms F745 SS (18Cr-12.5Ni-2.5Mo stainless steel) as a biomaterial, since it is less susceptible to localised corrosion in body-simulated fluids. In addition, the electrochemical response of DSS is superior to that of 316LVM (vacuum melt) and nickel free high nitrogen austenitic stainless steels alloyed with Mn, which are commonly employed in the medical industry [5].

In addition to the investigation of DSS corrosion resistance (2205 alloy) in as built condition [31,32], many experimental studies focused on coating the biomaterial by the electrophoretic deposition of a hydroxyapatite/titania nanocomposite [16] and by electrical discharge [15] to enhance the DSS biological response and corrosion resistance. Kose et al. [31] investigated the corrosion resistance and apatite formation on the surface of base and laser-welded AISI 2205 DSS implants in SBF for 1, 3, 7, 14, 21, and 28 days. The samples were laser-welded using the following values of laser power [W] and scanning speed [cm/min]: C1-3500 W, 90 cm/min; C2-3500 W, 270 cm/min; C3-4000 W, 90 cm/min, and C4-4000 W, 180 cm/min. The results indicate that apatite development was better on the surface of the base material in comparison with laser-welded samples, thus resulting in greater bioactivity. However, all of the samples kept in SBF exhibited extremely low corrosion rates (Figure 5A) due to their extremely minimal weight loss (Figure 5B). Therefore, laser-welded AISI 2205 DSS shows sufficient corrosion resistance for short-term implants in the human body depending on heat input [31].

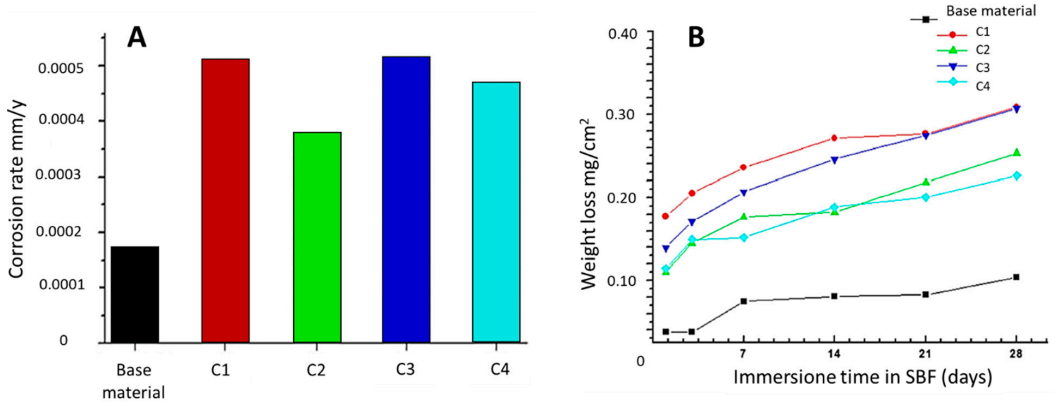


Figure 5. Corrosion behavior of AISI 2205 DSS base material and laser-welded samples (C1, C2, C3, and C4) during 28 days of SBF bath: (**A**) Corrosion rates; (**B**) Weight loss rates. Figures adapted with permission from [31]. Copyright (2020), Springer Nature.

Platt et al. [32] compared the corrosion behaviour of 2205 DSS to that of AISI 316L SS, subjecting both stainless steels to electrochemical and immersion corrosion tests in 0.9 wt.% sodium chloride solution at 37 °C. Electrochemical testing indicated that 2205 has a longer passivation range than 316L. When 2205 was coupled to 316L with equal surface area ratio, the corrosion rate of 2205 reduced, demonstrating that 316L acted like a sacrificial anode. When 316L is coupled with titanium-nickel (NiTi), titanium-molybdenum (TMA), or stainless steel arch wire, and is subjected to the immersion corrosion test, 316L stainless steel suffered from crevice corrosion. On the other hand, 2205 stainless steel did not show any localized crevice corrosion, although the surface of 2205 was covered with corrosion products, formed when coupled to NiTi and stainless steel wires. From the standpoint of corrosion resistance, the use of 2205 as an orthodontic bracket material seems to be justified when the arch wire material is stainless steel or titanium. The use of this alloy could decrease the amount of corrosion products to which a patient would be exposed that could minimize nickel allergy problems, which is potentially associated with orthodontic treatment [32].

Hammood et al. [16] investigated the electrophoretic deposition (EPD) of hydroxyapatite/titania (Hap/TiO_2) nanocomposites on 2205 DSS. Using the EPD process at a voltage of 30 V for 1 min, a homogeneous and crack-free thin coating was obtained. The Hap/TiO_2

nanocomposite coating on 2205 DSS showed the lowest corrosion current density and the best corrosion resistance in Ringer's solution. Furthermore, the coating displayed enhanced pitting corrosion resistance compared to the uncoated substrate when immersed in Ringer's physiological solution. Therefore, the results demonstrate that DSS offers superior corrosion resistance and stability, and is therefore suitable for medical applications as a substrate coated with a Hap/TiO_2 layer [16].

Similarly, Hammood et al. [7] examined a hydroxyapatite (Hap) coating on 2304 duplex stainless steel (DSS) through an EPD process, testing the corrosion behavior in simulated body fluid (SBF) through a potentiodynamic polarization. The Hap coating on the 2304 DSS, obtained at 30 V of voltage for 2 min, exhibits the higher corrosion resistance in SBF with respect to the uncoated samples, as is visible from the potentiodynamic polarization curves reported in Figure 6, and promotes good biocompatibility [7].

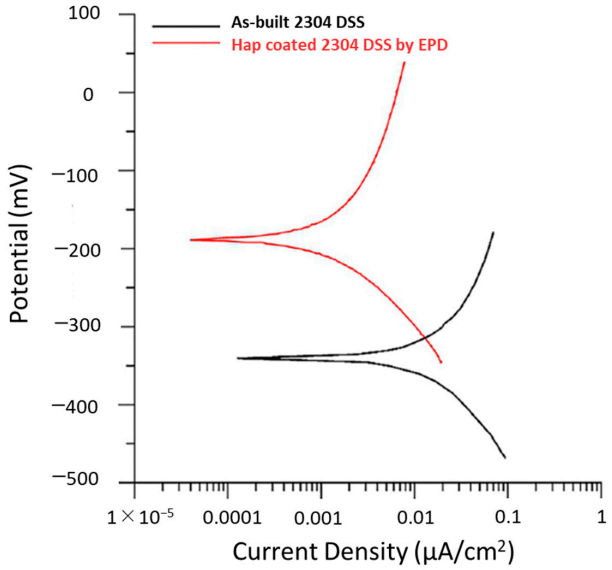


Figure 6. Potentiodynamic polarization curves of 2304 DSS in as-built and EPD conditions in an SBF solution at 37 °C. Figure adapted from [7].

A further surface treatment to improve DSS biological responses and corrosion resistance was performed by Mahajan et al. [15], focusing on the electrical discharge treatment of 2205 DSS. Electrical discharge machining (EDM) was carried out at various spark energy levels by varying input factors, and corrosion performances of unmachined and treated surfaces were studied through an electrochemical potentiodynamic test. Moreover, the biological behavior of unmachined and treated specimens was investigated by evaluating the in vitro interaction with human red blood cells. According to the results, EDM surface treatment considerably improves the corrosion resistance and biological properties of the DSS alloy. Therefore, the surface modification of 2205 DSS by EDM is regarded as a potential method for enhancing the corrosion resistance and biological responses that are necessary for biomedical applications [15].

Using electrochemical techniques, Sathiyanarayanan et al. [27] compared the corrosion behaviour of Ti6Al4V titanium alloy, conventional 22Cr-5Ni-3Mo-0.15N-0.02C DSS, (UNS 31803) and AISI 304 austenitic SS in synthetic biofluids, and commented on the suitability of DSS for use in biomedical applications. Their findings indicated that the general corrosion resistance of DSS is slightly lower than that of austenitic SS and a titanium alloy. However, when exposed to synthetic biofluids, DSS shows no signs of pitting, and exhibits exceptional resistance to localized corrosion on par with a titanium alloy. Thus, from the dissolution studies conducted on DSS in the Hank and Cigada solutions, it can be concluded that duplex stainless steels are one of the best alternates to titanium alloys, keeping the high cost factor in mind [27].

Table 1. In vitro performances of duplex and austenitic stainless steels studied and compared in the literature for biomedical applications. SS-stainless steel; ASS-austenitic stainless steel; DSS-duplex stainless steel.

Stainless Steels	Degradation Test	Mechanical Behavior	Magnetic Behavior	Reference
· 25Cr-7Ni-4Mo-N DSS (SAF 2507-UNS S31050) · 23Cr-4Ni · 22Cr-5Ni-3Mo DSS (SAF 2205-UNS S32205) · AISI 316L ASS · ASTM F138 ASS · 27Cr-31Ni-3.5Mo ASS	The resistance of the tested steels to localized corrosion in artificial physiological solution is as follows: 23Cr-4Ni < AISI 316L < ASTM F138 < 22Cr-5Ni-3Mo < 27Cr-31Ni-3.5Mo < 25Cr-7Ni-4Mo-N	–	–	[6]
		25Cr-7Ni-4Mo-0.28N DSS shows fatigue limits remarkably higher than ASTM F138 ASS	–	[28]
· 25Cr-7Ni-4Mo-N DSS · 18Cr-12.5Ni-2.5Mo (F745 SS-ASTM F745)	25Cr-7Ni-4Mo-N DSS suffers lower susceptibility to localised corrosion in body simulated media than F745 SS	UTS and YS values for the DSS were 870 and 560 MPa, while they were 460 and 220 MPa for the F745 SS, respectively; while F745 SS shows higher elongation (30%) than DSS (20%)	DSS shows higher magnetic saturation and remanence, whereas F745 SS has a higher coercive force	[5]
· SAF 2507 DSS · SAF 2205 DSS	SAF 2507 exhibits higher corrosion resistance in artificial saliva than SAF 2205, both before and after heat treatment			[17]
2205 DSS coated with hydroxyapatite/titania (Hap/TiO_2) nanocompositeusing EPD process	Coating deposited (Hap/TiO_2 nanocomposite) exhibits improved pitting corrosion resistance when immersed in Ringer's physiological solution with respect to uncoated 2205 DSS			[16]
2304 DSS coated with hydroxyapatite (Hap) through EPD process	The Hap coating on the 2304 DSS has higher corrosion resistance in SBF than the uncoated samples			[7]
AISI 2205 DSS	Very low corrosion rates due to very low weight losses were detected in all samples kept in SBF at different times			[31]
· 22Cr-5Ni-3Mo-0.15N-0.02C (UNS 31803) · AISI 304 austenitic SS	The general corrosion resistance of DSS is slightly inferior to that of austenitic SS; however, DSS does not show any signs of pitting when exposed to synthetic biofluids, and exhibits excellent resistance to localised corrosion			[27]
2205 DSS treated with Electrical discharge machining (EDM)	The surface treatment by EDM significantly enhances the corrosion resistance and biological performances of 2205 DSS			[15]
· 2205 DSS · AISI 316L SS	2205 has a longer passivation range than 316L in a sodium chloride solution			[32]

2.1.2. Mechanical Behavior

Surgical implants are vulnerable to dynamic loads exerted by body movements and weight. During walking, the load of an implant can reach four times the body weight at the hip and three times the body weight at the knee. Although the static test does not reflect the actual working conditions of the implants, it allows for the behaviour comparison of different biomaterials and for the making of an estimation of their final performance [5].

Comparing the mechanical properties of 25Cr-7Ni-4Mo-N DSS and 18Cr-12.5Ni-2.5Mo SS (F745 SS), the ultimate tensile strength (UTS) and yield strength (YS) values were 870 MPa and 560 MPa for the first, and 460 MPa and 220 MPa for the second, respectively (Figure 7). The higher mechanical strength of the DSS with respect to F745 SS is not directly related to the balance of the austenite and ferrite properties, since UTS and YS show greater values than those of both phases. The increase in mechanical strength can be attributed to the smaller grain size, which typically possesses DSS, in addition to the solid solution hardening encouraged by the higher substitutional Cr and Mo concentrations, in addition to the interstitial N. Moreover, UTS and YS are directly related to the fatigue strength; therefore, the higher values of these parameters reported for DSS indicate that this material has greater fatigue resistance than F745-SS and, subsequently, a lower probability of mechanical failure [5].

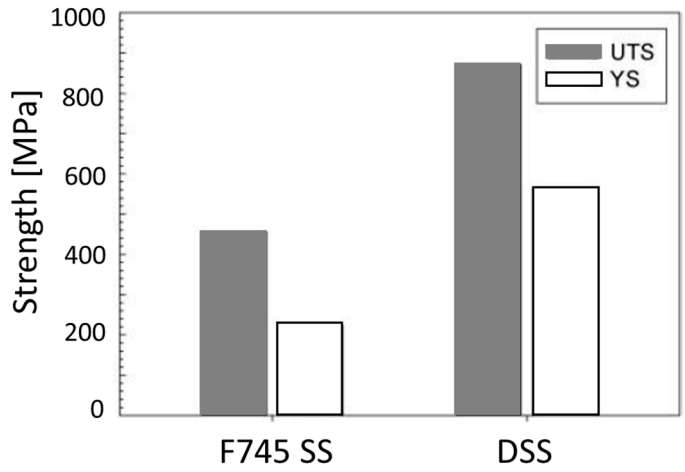


Figure 7. Comparison of mechanical values between 25Cr-7Ni-4Mo-N DSS and 18Cr-12.5Ni-2.5Mo SS (F745 SS) in solution annealed conditions. UTS—ultimate tensile strength; YS—yield strength. Figure adapted with permission from [5]. Copyright (2015), Taylor & Francis.

This result is consistent with the findings of Cigada et al. [28], showing that the fatigue limits of 25Cr-7Ni-4Mo-0.28N DSS can be significatively higher than those of the ASTM F138 austenitic SS. This makes it easier to predict a better in vivo behaviour of prosthetic components produced with the DSS compared to the traditional one [28]. In contrast, the elongation values were 20% for DSS and 30% for F745 SS. The greater elongation of F745 SS is a result of its fully austenitic structure, which confers higher ductility. In the case of DSS, the presence of ferrite in the microstructure reduces its ductility, while increasing its mechanical strength [5].

2.1.3. Magnetic Behaviour

The knowledge of the magnetic behaviour of biomaterials is essential, since exposure to static and/or variable magnetic fields (e.g., magnetic resonance imaging—MRI), may result in heat or movement that can be harmful to the human body. For example, the field strengths of MRI scanners range from 0.2 to 7.0 T, with the majority operating at 1.5 T. The main inconveniences that can occur in this environment are magnetically induced displacement forces and torques, as well as heating and image artefacts [5].

The magnetic properties of 25Cr-7Ni-4Mo-N DSS and F745 SS were analysed by Gregorutti et al. [5]. The magnetic analysis found that both stainless steels exhibit properties similar to those of soft magnetic materials. The most significant differences are magnetic saturation and remanence, which are greater in DSS due to the presence of ferrite in its microstructure. However, F745 SS shows a higher coercive force, indicating that it is more susceptible to heating when exposed to magnetic fields [5].

The ferritic phase of DSS shows excellent magnetic properties, which proved their applicability in endoprosthetics as biomaterials for magnetic stents [15], but prevented their acceptance as implant materials [30].

2.2. In Vivo Experiments

In vivo biological tests aim to understand the DSS behavior when in contact with biological tissues. The suitability of DSS for the manufacturing of osteosynthesis devices or orthopedic components in place of the traditional austenitic SS [28,33], and for the induction of interstitial hyperthermia in deep-seated tumors [34], was investigated by the in vivo experiments listed in Table 2.

Table 2. In vivo experimental works in the literature that used duplex stainless steels.

Stainless Steels	Experimental Study	Reference
· 25Cr-7Ni-4Mo-0.28N DSS · AISI 304L · ASTM F138 austentic SS	Crevice corrosion investigation of implant on rabbit and sheep femurs and of Endomedullary nails (Ender type) in patient femurs for about 6 months, to set up an alternative to the employ of conventional austenitic SS	[28]
	Cylindrical pin (2 mm diameter, 6 mm length) implantation in rabbit for 6 and 12 months to find an alternative with respect to the ASTM F138 austenitic SS	[33]
· 16.5Cr-9.5Ni-5.3Nb-4Cu-3.2Co DSS	Thermoseed (0.23 mm diameter, either L-shaped and I-shaped) insertion in the liver of New Zealand white rabbits for inducing heating by magnetic field exposition to cause hyperthermia	[34]

Cigada et al. [28] conducted an in vivo investigation on sheep and rabbits to evaluate the biocompatibility and the in vivo localized corrosion resistance of 25Cr-7Ni-4Mo-0.28N DSS. After the implant, the rabbit and sheep femur sections revealed a certain bone growth close to the metal device, without interposed connective tissue. The bone near the implant exhibited no metallic ion diffusion, and the phosphorus/calcium ratio (P/Ca) in the new bone was comparable to that of the old bone. With regard to the testing on special localized corrosion devices, either after 26 weeks or after 52 weeks implantation time, the tests showed pitting corrosion on the AISI 304L, crevice corrosion on the ASTM F138 austentic SS, but no corrosion at all on the 25Cr-7Ni-4Mo-0.28N DSS [28].

Cigada et al. [28] subsequently carried out a preliminary clinical investigation based on these in vivo results on animals. As a typical application, the osteosynthesis of the lateral fracture of the femoral neck with the insertion of two or more Ender-type endomedullary nails was selected. Some patients were implanted with 4.5 mm diameter nails, fabricated with cold-worked 25Cr-7Ni-4Mo-0.28N DSS and ASTM F138 steel, for a period of six months. After the fracture had successfully healed, the Ender nails were withdrawn. A substantial portion of implanted traditional Ender nails manufactured from ASTM F138 steel exhibits severe crevice corrosion which originated from the contact zone between the nails. On the other hand, when 25Cr-7Ni-4Mo-0.28N DSS was utilized, the fretting was minimal and the crevice corrosion was non-existent [28].

Furthermore, cylindrical pins (2 mm diameter and 6 mm length) of the these two latter materials were implanted in the femurs of rabbits by Cigada et al. [33]. In addition, a device was designed to test the in vivo resistance to the localized corrosion of ASTM F138 and 25Cr-7Ni-4Mo-0.28N DSS. This device comprised two metallic disks sandwiched between

two PTFE disks. This anti-corrosion device was implanted in the trochanteric region of the femurs. After 12 months, trabecular bone completely surrounded the pins, showing a close contact between the metal and bone and the presence of many vascular cavities in the bone at the metal interface (Figure 8A). No significant differences were observed in bone regrowth and vascularization of the two steels (ASTM F138 and 25Cr-7Ni-4Mo-0.28N DSS). The analyses performed close to the duplex pins detected only Ca and P, whereas small amounts of Fe and Cr were found near the austenitic pins. Additionally, pitting corrosion was identified on the AISI 304 austenitic SS, crevice corrosion was detected on the ASTM F138 austenitic SS, and no corrosion at all was observed on the 25Cr-7Ni-4Mo-0.3N DSS. The main corrosion attacks occurred at the metal/PTFE interfaces [33].

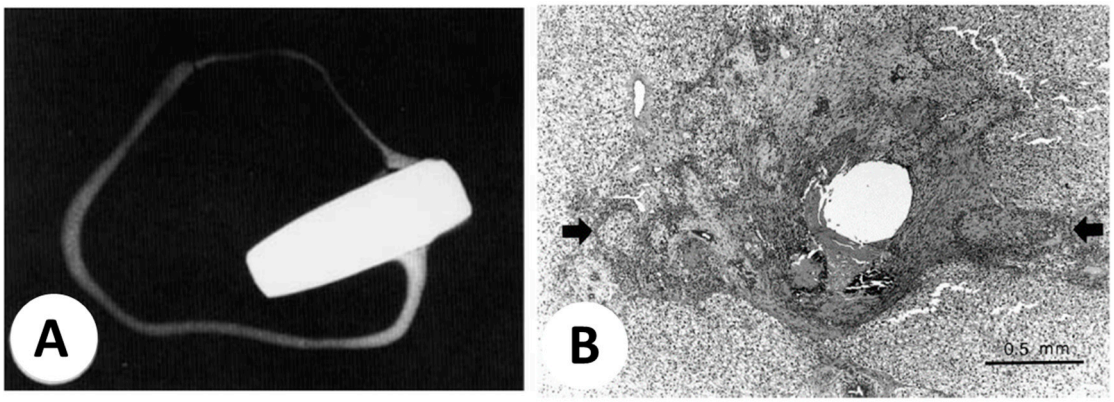


Figure 8. Micrographs of (**A**) femur cross sections containing the 25Cr-7Ni-4Mo-0.28N DSS cylindrical pin 12 months after the implantation, and (**B**) rabbit liver after the induction of interstitial hyperthermia (7 days) using a 16.5Cr-9.5Ni-5.3Nb-4Cu-3.2Co DSS thermoseed. The area of coagulation necrosis of about 4 mm in diameter is indicated by arrows. The figures were adapted from [28] and [34], respectively.

In conclusion, the in vivo results demonstrated that the 25Cr-7Ni-4Mo-O.3N duplex stainless steel is not susceptible to crevice corrosion in the human body, at least under static conditions, and that it can be considered a good biocompatible material.

However, DSS (16.5Cr-9.5Ni-5.3Nb-4Cu-3.2Co wt.%) was also used to induce hyperthermia in rabbit liver for the treatment of cancer, as it produces temperature-dependent heat in the presence of an external magnetic field. By heating a DSS thermoseed with an external magnetic induction field, Park et al. [34] induced localized interstitial hyperthermia without connecting the thermoseed to a power source. Metal thermoseeds generate heat through eddy current loss, and nearby tissues are heated by thermal conduction. Thermoseed in the form of a 0.23 mm diameter wire (either L-shaped 4 cm long, or I-shaped, 2.5 cm long) was inserted in the liver of New Zealand white rabbits. To generate interstitial hyperthermia, the rabbit was placed in the center of an induction coil for 30 min while 5.4 kW of power was supplied to the induced magnetic field. Coagulation necrosis occurred around the insertion site to a variable extent, but was most severe at the central portion (Figure 8B). According to Park et al. [34], this relatively small extent of coagulation necrosis can be increased by (i) increasing the radius of the thermoseed; (ii) employing multiple thermoseeds simultaneously in a square grid pattern; (iii) extending heating time; (iv) utilizing a stronger magnetic induction field, or (v) using thermoseeds with a higher Curie point. In conclusion, the newly designed thermoseeds in the DSS exhibited acceptable temperature and temperature-dependent heating properties, inducing coagulation necrosis in rabbit liver. Thus, it can be concluded that duplex stainless steel is a novel material suitable for the manufacturing of thermoseed for inducing interstitial hyperthermia.

3. Laser Powder Bed Fusion (LPBF) of DSS

In recent years, a growing number of studies have focused on the design and modification of alloy powders for additive manufacturing (AM) via the in situ alloying of powder mixes in order to produce the desired microstructures and properties. In addition, the effect of AM processing parameters and post-treatments on the microstructural development (namely the two-phase ratio and precipitates), mechanical characteristics, and corrosion resistance have been studied extensively in the literature [8].

3.1. Relative Density and Defects

The lack of fusion and residual porosity are typical flaws in DSS produced by additive manufacturing that must be avoided, given their detrimental influence on the mechanical behavior. As can be seen in Figure 9A,B, the lack of fusion results in uneven voids between scan tracks and layers, which is the effect of inadequate heat input causing incomplete fusion. [35]. This flaw may be removed by increasing the laser energy input [36]. Davidson et al. [36] investigated the influence of volumetric energy density (VED) on formation quality 2507 DSS [36]. The volumetric energy density (J/mm^3), VED, is a synthetic index for describing the physical meaning of the L-PBF process [37]:

$$VED = \frac{P}{vht} \quad (1)$$

where P is the laser power (W), v is the scan speed (mm/s), h is the hatch distance (mm), and t is the layer thickness (mm). There are two major types of pores (and related formation mechanisms) in metal additive manufacturing: metallurgical pores and keyhole pores [38,39]. Most of the metallurgical pores in L-PBF are caused by unfused powder particles (Figure 9A) or trapped shielding gas (Figure 9B), the latter giving rise to perfectly spherical pores (Figure 9B) [40,41].

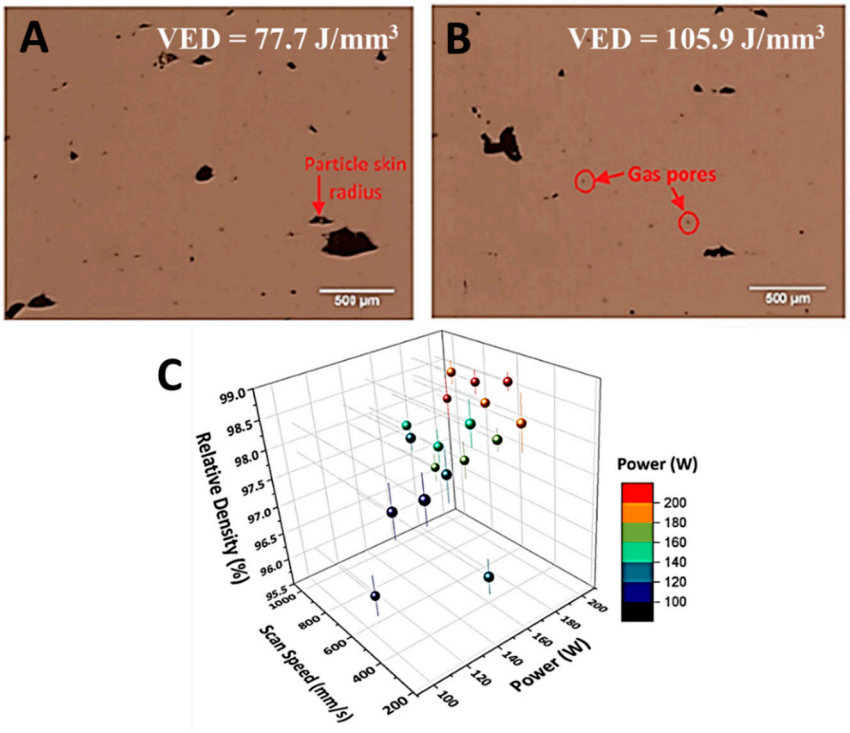


Figure 9. The effect of L-PBF processing conditions on DSS: (**A**,**B**) Pore morphology on a 2507 alloy at different VED. Figures adapted with permission from [8]. Copyright (2022), Elsevier; and (**C**) Relative density of a 2205 alloy by varying scan speed and laser power. Figure adapted with permission from [42]. Copyright (2021), Elsevier.

A similar result was found for 2205 DSS by Nigon et al. [42]. The highest relative density (98.6%) was obtained with 187 W of laser power and 800 mm/s of scanning speed (VED = 156 J/mm^3), as shown in Figure 9C. In terms of process optimization, insufficient energy input leads to a lack of fusion, while excessive energy input results in keyhole porosity; high densification can only be achieved using an adequate level of energy input (Figure 9C). Under inadequate energy input during the L-PBF process, keyholes are repeatedly generated and collapsed, leaving blowholes containing metal vapor or shielding gas within the deposited metal. The size and shape of keyhole pores are mainly driven by the L-PBF printing conditions. If pores form on the surface, they become the natural beginning sites for pit corrosion, hence reducing the corrosion resistance [8].

In addition to a precise control of the VED (laser power of 250 W), Papula et al. [43] achieved 2205 DSS samples with a full density by adjusting the scanning strategy with 66° rotation between layers [43]. The density was 99.97% based on the applied process parameters and the 66° rotation in the scanning direction between consecutive layers (Figure 10A). Lower density (99.01%) and much bigger pores were seen in the non-rotated scanning strategy sample (Figure 10B).

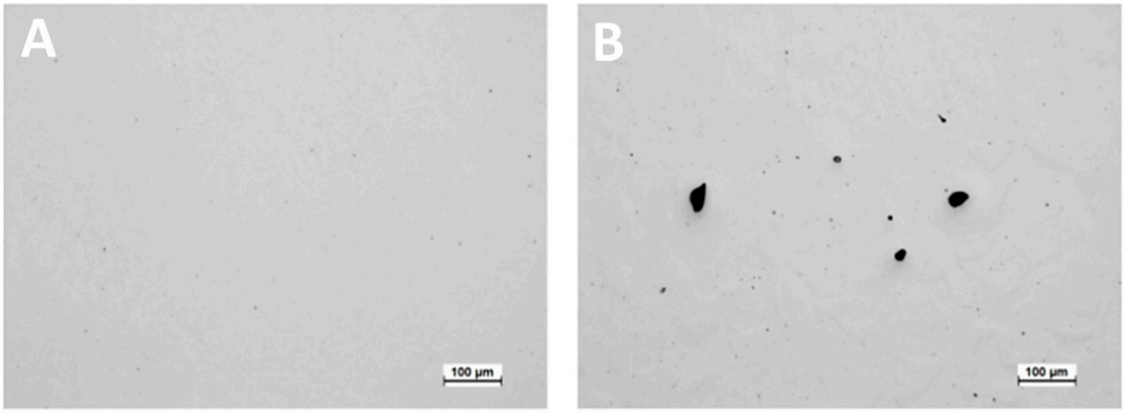


Figure 10. Optical micrographs of (**A**) 2205 DSS as-built sample treated with 66° rotation in the direction of scanning, and (**B**) an as-built sample processed without rotation in the direction of scanning between the layers. The figures are adapted from [43].

To enhance the relative density, experimental studies have also focused on the heat treatments applied to L-PBF DSS (Fe-22Cr-5Ni-0.26N). Hongliang Xiang et al. [44] investigated L-PBF high-density specimens subjected to solution treatments at three different temperatures (1000, 1100 and 1200 °C) for a dwell time of 1 h. Few residual micropores can be seen in the macrostructure of the as-built specimen (Figure 11A). Following solution treatment, the specimens' relative densities increased by between 0.2% and 0.4%. (Figure 11B). Hence, solution treatment can enhance the relative density of the samples. Austenite has a denser atomic structure than ferrite, and therefore increasing the quantity of the austenitic phase might improve the specimen's density [45]. Therefore, the solution treatment enhanced the austenite concentration and, as a result, the relative density of the DSS specimens manufactured by L-PBF [8,33–44].

Arumughan Akilan et al. [46] took advantage of hot isostatic pressing (HIP) to improve the density of L-PBF 25Cr7Ni DSS samples, hence enhancing the performance of the components [46]. The relative density of the as-printed samples increased following HIP treatment at HIP1000 and HIP1170, respectively (Figure 12). Figure 12A depicts a polished optical micrograph of the as-printed L-PBF sample along the build direction ZX, which mostly reveals irregular voids caused by unmelted powders. The micrographs highlighted the lack of fusion defects and revealed large irregular voids that span across multiple layers (Figure 12A). As a result of the HIP treatment, the total porosity of as-printed samples decreased from over 5.4% to less than 0.1% (Figure 12B,C) [46].

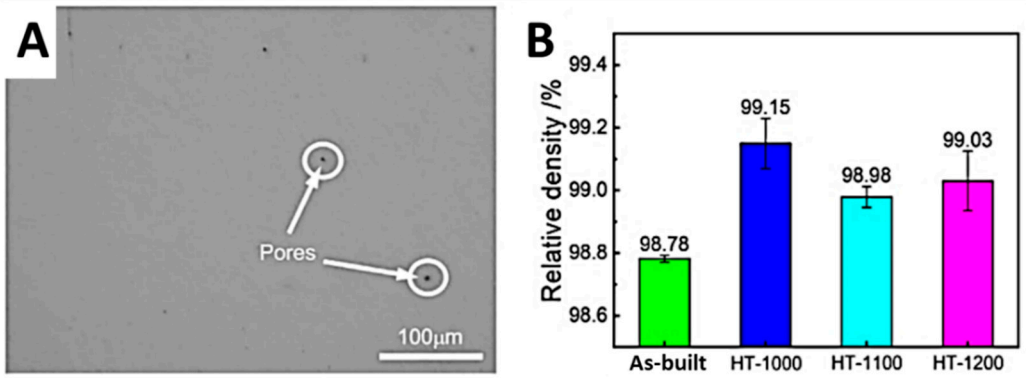


Figure 11. Heat treatment effects on DSS samples manufactured by L-PBF: (**A**) Optical macrostructure of an as-built sample; and (**B**) the relationship between solution treatment and relative density [44].

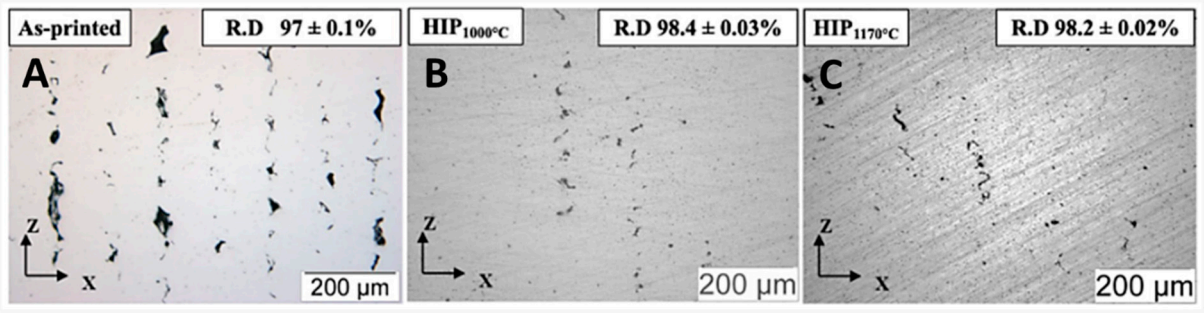


Figure 12. Optical micrograph of 25Cr7Ni DSS produced by L-PBF: (**A**) as-printed sample along the build direction ZX, (**B**,**C**) as-printed samples after HIP treatment at HIP_{1000} and HIP_{1170}, respectively. The figures are adapted from [46].

3.2. Microstructure Evolution

Given the typical cooling rates of the L-PBF technology, which are in the range of 10^5 K/s and 10^6 K/s [35], the fabrication of DSS components can lead to a variety of microstructures and, most importantly, to peculiar ratios of austenite and ferrite in duplex stainless steels. The components of the as-deposited standard (UN S32205) and super (UNS S32505) DSS alloys exhibit ferritic microstructures with primary austenite grain boundaries and very little intragranular austenite at these cooling rates [27,39,47]. The grain size value of the L-PBF components is mostly governed by the cooling rate during the solidification phase. As reported by Murkute et al. [48], the average grain size decreased from 110 to 20 μm^2 when the scan speed was increased from 100 to 1000 mm/s during the L-PBF of DSS 2507 [48]. A high cooling rate refines grains, thus improving both strength and ductility, while having a considerable impact on corrosion resistance at the same time [49]. As the ferrite phase arises immediately during solidification, its grain morphology (M) is dictated by the ratio of the temperature gradient (G) and solidification rate (R) at the front of solidification (M = G/R). Columnar grains have a high G/R ratio, whereas equiaxed grains have a low G/R ratio [8,50,51]. In general, the primary ferrite in DSS exhibits a columnar morphology. After solidification, the ferrite converts into austenite via solid transformation. The addition of post-process isothermal heat treatments increases the austenite fractions, resulting in a more balanced ferrite/austenite microstructure. The super duplex stainless steel 2507 was printed by Davidson et al. [36] using fixed process parameters, except for the laser power. Because of the high cooling rates, instead of an austenitic-ferritic microstructure, a pure ferritic microstructure was found after the L-PBF procedure. Following complete solution annealing, the balanced inner microstructure (45% austenite) was recovered; however, the austenite phase showed a "needle-like" morphology [36]. In a further experimental study, Davidson et al. [41] performed a matrix of laser power and laser volumetric energy

densities (VED) to clarify the process-microstructure relationship of 2507 DSS manufactured by L-PBF. The L-PBF process distorts the equilibrium and resulting duplex stainless steels with a primarily ferritic microstructure [26]; this factor is essential for the creation of soft magnetic materials, as well as mechanical strength and chemical resistance. Specifically, as visible from Figure 13A, the microstructures of L-PBF DSS samples show the austenite phase as dark lines along grain boundaries, and as Widmanstätten needles inside the ferrite matrix, whereas the dark area represents a lack of fusion (Figure 13A). Additionally, the average values of the ferrite content decrease with the increase in the volumetric energy density value [26], as shown in Figure 13B. The maximum ferrite content of 73% observed at 50 J/mm^3 is comparable with the average ferrite content of 75–78% reported by Saeidi et al. for SAF 2507 DSS L-PBF using the following process parameters: a laser power of 190 W, a scan speed of 750 mm/s, and a hatch distance of 0.1 mm [52]. Thus, it is evident that the DSS produced by L-PBF has an average ferrite content of about 70%, which is characteristic of the rapid cooling rates impairing the austenite growth [26].

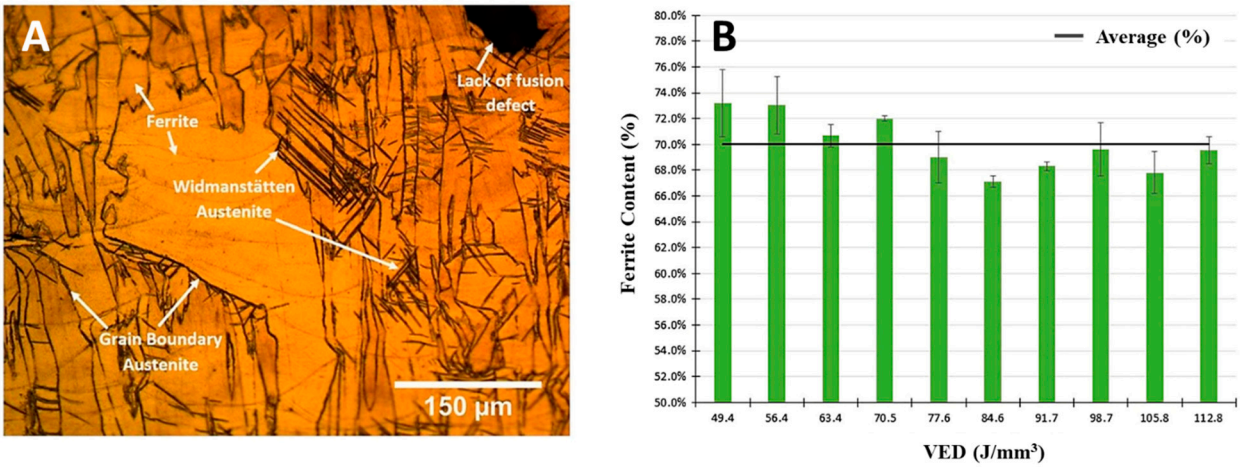


Figure 13. L-PBF DSS microstructure analysis: (**A**) Optical micrographic showing the austenite phase (dark lines along grain boundaries and as Widmanstätten needles) in a ferrite matrix. The dark area represents a lack of fusion; and (**B**) Diagram of ferrite content (%) versus VED. The figures are adapted with permission from [26]. Copyright (2016), Springer Nature.

Hengsbach et al. [47] described the as-built state of UNS S31803 DSS processed by L-PBF as a completely ferritic microstructure. The grain morphology, detected by the electron backscattered diffraction (EBSD) maps reported in Figure 14A,B, is characterized by elongated grains, which suggest an isotropic microstructure resulting in epitaxial grain growth. The formation of austenite and other precipitations is completely suppressed in the as-built state, due to process-related high cooling rates [47]. Heat treatments ranging from 900 °C to 1200 °C for 5 min to obtain the desired balanced austenitic-ferritic microstructure (Figure 14C,D) were performed by Hengsbach et al. [47], and the results of transmission electron microscopy (TEM) observations revealed that a high dislocation density is induced by the L-PBF process (Figure 14E), while a recrystallized microstructure prevailed after the heat treatment (Figure 14F).

The austenite volume fraction (Figure 15) reaches the maximum content (34 vol%) at an annealing temperature of 1000 °C, while the austenite volume steadily decreases (24 vol%) by decreasing the annealing temperatures to 900 °C [47].

The work of Hengsbach et al. [47] demonstrated the effective fabrication of a duplex stainless steel by laser powder bed fusion with a substantially balanced austenite-ferrite arrangement. As high cooling rates inhibit austenite nucleation in the as-built condition, the microstructure is nearly entirely ferritic. After heat-treating the specimens, a microstructure composed of secondary austenite and delta ferrite recrystallizes in contrast to the as-built

state. The occurring recrystallization can be elucidated by the high dislocation density (lattice defect), induced during L-PBF processing [47].

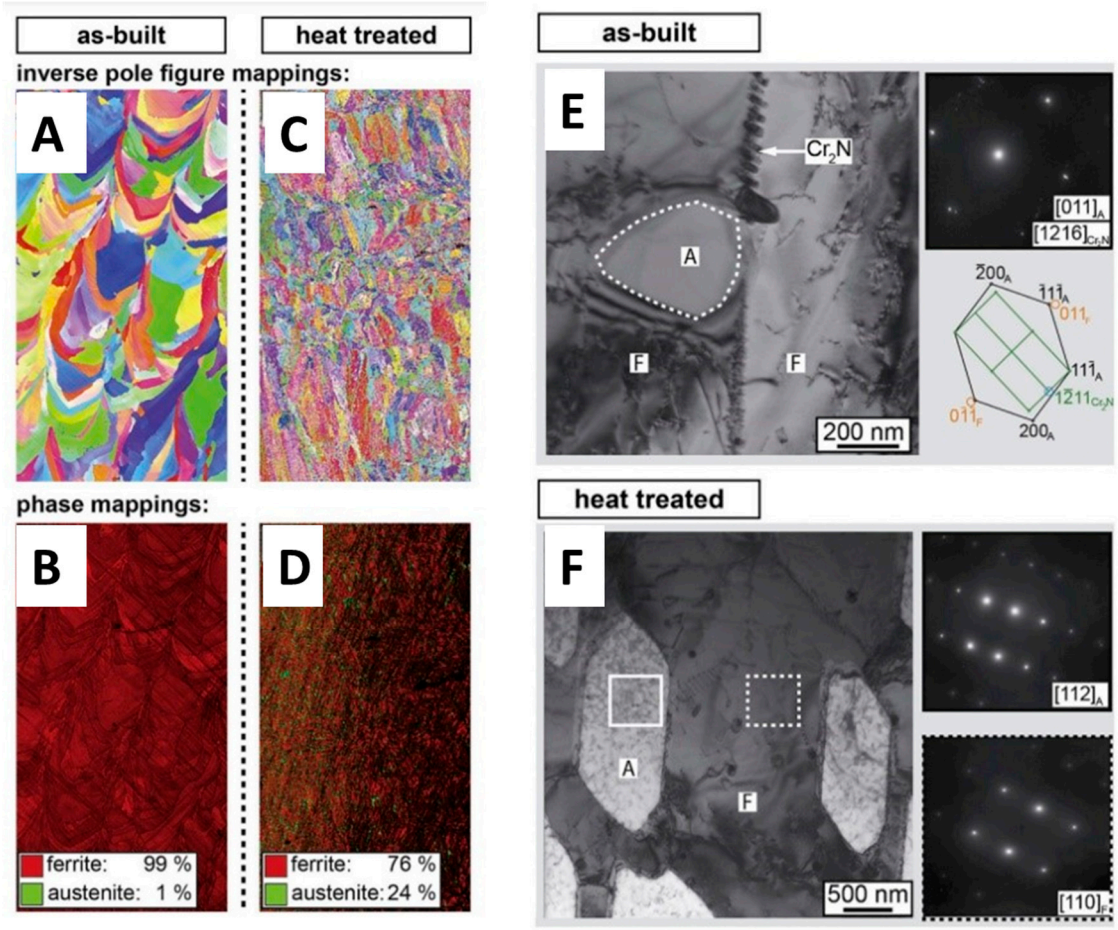


Figure 14. Microstructure analysis of UNS S31803 DSS processed by L-PBF: (**A–D**) EBSD inverse pole figure and phase mappings of the same material. The microstructure is almost fully ferritic in the as-produced state, with small austenite grains and chromium nitride precipitates along the grain boundaries (**A**,**B**). A suitable heat treatment partially recovered the desired duplex austenite/martensite microstructure (**C–F**) the TEM images of the as-produced state and in the heat-treated state. The figures are adapted with permission from [53]. Copyright (2020), Elsevier.

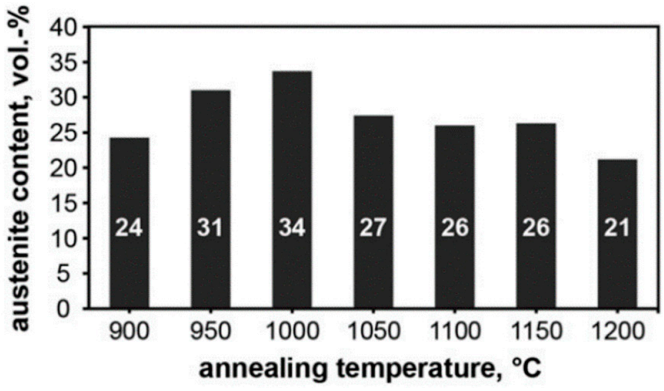


Figure 15. Austenite phase content (vol%) quantified via EBSD phase mapping in annealed DSS by L-PBF. Figure adapted with permission from [47]. Copyright (2017), Elsevier.

In addition, Suvi Papula et al. [43] analysed the microstructure of L-PBF 2205 DSS in the as-built and heat-treated (1000 °C/5 min, 1050 °C/5 min and 1000 °C/60 min) conditions, through EBSD inverse pole figures (Figure 16A,C,E,G) and phase maps (Figure 16B,D,F,H) [43]. Figure 16A,B depicts the construction-aligned columnar grain morphology of the as-built samples. The AM-processed samples exhibit epitaxial growth as a result of the distribution of columnar grains into successive layers. The as-built 2205 DSS showed a 100 vol% ferritic solidification microstructure due to the fast cooling rates, while the nucleation and recrystallization of the austenite was primarily driven by the high dislocation density of as-fabricated DSS specimens was detected after the heat treatments [43]. Around forty percent of the austenite is formed at annealing temperatures between 950 °C and 1150 °C (Figure 16), with the highest austenite concentration recorded between 1000 °C and 1050 °C [43]. Suvi Papula et al. [43] concluded that the as-built specimen has a high yield and tensile strength, but a lower ductility. Due to the microstructure's tiny phase size [54], the tensile and yield strength values of heat-treated DSS specimens are much greater.

Nigon et al. [42] compared 2205 DSS parts built via L-PBF in as-built and annealed states. Figure 17 depicts the recovery of the DSS microstructure by solution annealing at 1100 °C for one hour in air, followed by water quenching. The EBSD results reported in Figure 17 show a small austenite content in the as-built condition, but this result is still unclear, since it can be that the 0.7% residual austenite is a consequence of recrystallized austenite during the melting process or from measurement noise [42].

Hongliang Xiang et al. [44] analysed the effect of a solution treatment on the microstructure of L-PBF Fe-22Cr-5Ni-0.26N DSS. The as-built sample shows a 100% ferritic structure (Figure 18A), while after the application of solution treatments for 1 h at 1000, 1100, and 1200 °C, the austenite content decreases from 60.3 to 56.6% (Figure 18B–D). This suggests that the fractions of ferrite and austenite are highly dependent on the temperature of the solution treatment, with an increase in temperature resulting in a drop in the fraction of the austenite phase. The solution treatment can recover the two-phase structure, refine the grain size, weaken the texture, and decrease the dislocation content, thereby lowering the system's free energy and enhancing the microstructural stability [44].

In addition to the matrix phases of austenite and ferrite, secondary phases such as intermetallic compounds (σ and χ), nitrides (CrN and Cr2N), secondary austenite ($\gamma 2$), and carbides [55,56] may also form depending on the heat cycles performed and the remelting performed by the laser source during the L-PBF additive manufacturing processes. The formation of the σ phase mostly results from the eutectoid transition of ferrite ($\delta \rightarrow \sigma + \gamma 2$), and takes place between 600 and 1000 °C. The brittle σ phase is rich in Fe, Cr, and Mo, and often precipitates along the ferrite/austenite (δ/γ) phase boundary, or at triple junctions. Nevertheless, the formation of the σ phase during the L-PBF process has been seldom seen due to the high cooling rate, which limits its formation [57]. The presence of the σ phase lowered the toughness and ductility of the DSS but enhanced its tensile strength [58]. Davidson et al. [41] detected chromium nitrides (CrN) with spherical and acicular morphologies when processing 2507 DSS by L-PBF [41]. The nitrides cause the degradation of DSS's toughness and corrosion resistance [59]. By increasing the amount of austenite by the application of N_2 shielding gas or a solution heat treatment, more nitrogen is dissolved in the matrix, hence preventing the precipitation of nitrides [8].

In Table 3, the microstructural properties of DSS produced by the L-PBF technology are summarized.

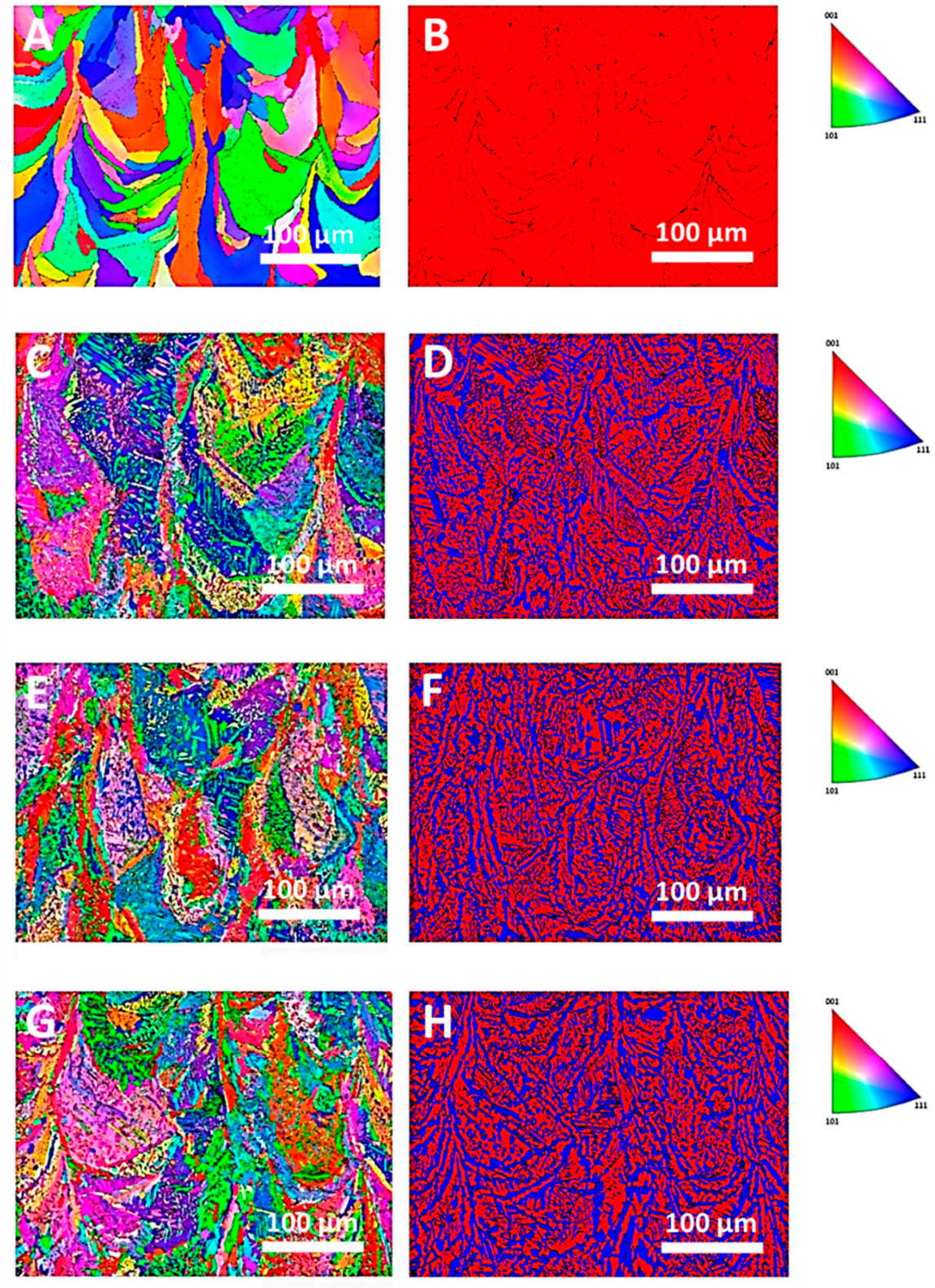


Figure 16. EBSD inverse pole figures (**A**,**C**,**E**,**G**) and phase maps (**B**,**D**,**F**,**H**) of the as-built specimen with 66° scanning rotation (**A**,**B**) and the heat treated specimen at 1000 °C/5 min (**C**,**D**), 1050 °C/5 min (**E**,**F**), and 1000 °C/60 min (**G**,**H**). The figures are adapted from [43].

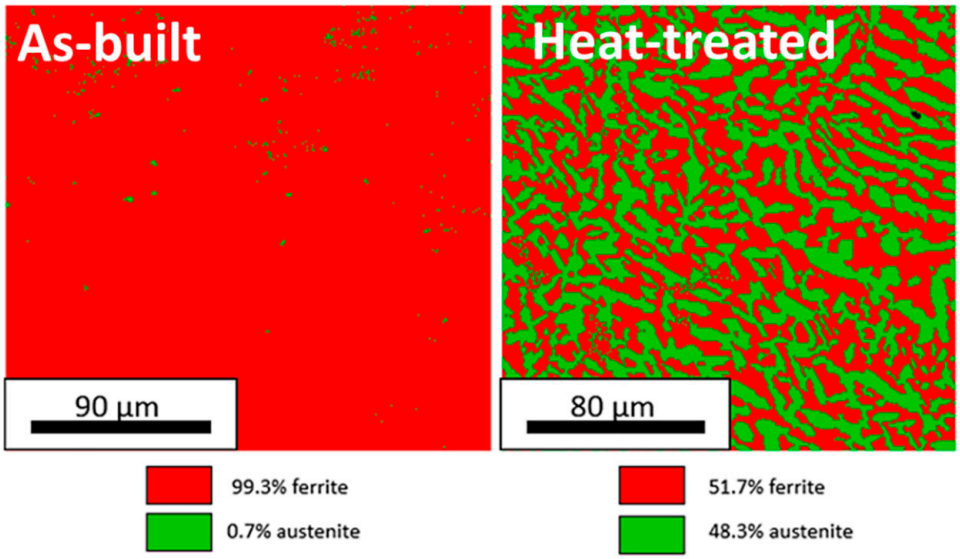


Figure 17. EBSD phase map for DSS 2205 processed by L-PBF in as-built and annealed conditions. Figure adapted with permission from [42]. Copyright (2021), Elsevier.

Table 3. Processing conditions and microstructural characteristics of DSS manufactured by L-PBF.

DSS	Reference	VED (J/mm^3)	Sample	Microstructure		
				Austenite Percentage (vol%)	Ferrite Percentage (vol%)	Secondary Phases
2205	[47]	59	as built HT 900 °C HT 1000 °C HT 1200 °C	1 24 34 21	99 76 66 79	Nitrides, γ2
2205	[42]	156	as built HT 1100 °C	0.7 48.3	99.3 0.7	–
2507	[52]	127	as built	22 ÷ 25	75/78	Nitrides
2507	[41]	91.7–141	as built	31.2	68.8	Nitrides
2507	[26]	84.6 112.8	as built	32.89 8.3	67.11 91.7	–
2507	[60]	133	HT 1200 °C	71	13	σ
2507	[48]	1333.33–133.33	as built	1.1–10.7	88.9–98.7	–
2205	[43]	–	HT 950 °C/5 min HT 1000 °C/5 min HT 1050 °C/5 min HT 1100 °C/5 min	40 43 43 43	60 57 57 57	–
Fe-22Cr-5Ni-0.26N	[44]	79	as built HT 1000 °C HT 1100 °C, HT 1200 °C	0.02 60.3 57.6 56.6	99.8 39.7 42.4 43.4	–

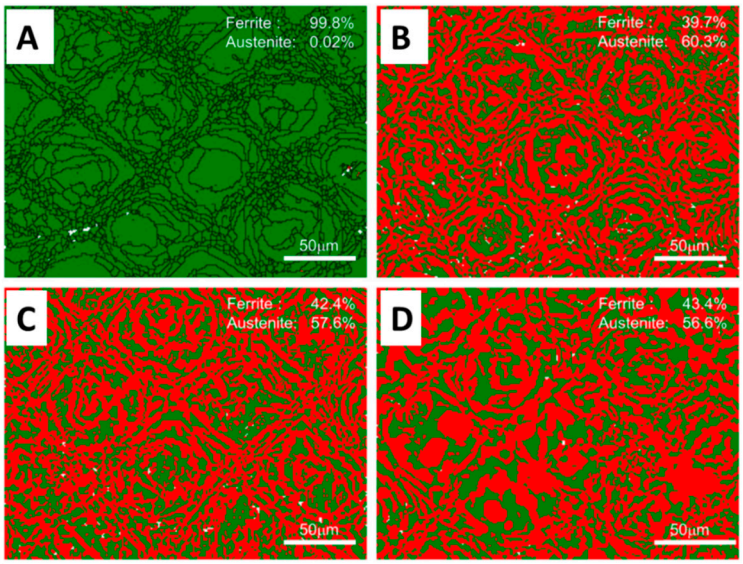


Figure 18. EBSD phase maps of the specimens: (**A**) As-built, (**B**) Heat-treated at 1000 °C for 1 h, (**C**) Heat-treated at 1100 °C for 1 h, and (**D**) Heat-treated at 1200 °C for 1 h. The green region represents the ferrite phase, the red area represents the austenite phase, and the white area indicates the area with no resolution. The figures were adapted from [44].

3.3. Evolution of Mechanical Properties

The microstructural arrangement and surface quality have a large impact on the mechanical characteristics of DSS components manufactured using L-PBF. Specifically, hardness and tensile strength are influenced by grain size, while the ductility and toughness are affected by the presence of tiny defects and by the limited austenite content [8]. Studies that focused on the mechanical properties of L-PBF DSS samples (hardness, tensile and fatigue tests) often reported also experimental results of forged DSS alloy with similar chemical compositions, for comparison.

3.3.1. Hardness

The hardness of DSS parts varies depending on the considered chemical composition and on the L-PBF processing conditions. The hardness of austenite and ferrite rises with the number of their dissolved alloying elements [61]. The diffusion of alloying elements is temperature- and cooling rate- dependent, leading to a redistribution of the chemical composition, microstructure, and, therefore, hardness. In particular, the main microstructural features influencing hardness are the following: (i) a two-phase ratio; (ii) the precipitation of secondary brittle phases and the formation of nitrides, which generally increases the hardness; and (iii) grain size, which partially explains the difference in hardness among various AM processing conditions [41]. The heat treatment has a substantial effect on the distribution of alloying elements, the two-phase ratio, and the secondary phases, and consequently has a significant impact on the hardness of samples fabricated by various AM techniques [8,43].

Nigon et al. [42] quantified the average hardness of 2205 DSS as 420 HV for the as-built samples of L-PBF, whereas the hardness of wrought 2205 DSS was 270 HV. After a solution heat treatment at 1100°C for 1 h, microhardness decreased to 260 HV [42]. Similarly, Davidson et al. [41] obtained a hardness value of 410 HV for L-PBF 2507 DSS specimens, resulting in an HV that was 125 HV higher than the wrought condition due to the particular microstructure and the presence of nitrides [41]. Suvi Papula et al. [43] observed that in the as-built condition, the microhardness of L-PBF 2205 DSS was higher than heat-treated and cold-rolled DSS with a similar chemical composition (Table 4). Following different heat treatments, the microhardness decreased, but its value was still higher than that of cold-rolled samples [43].

Table 4. Microhardness (HV) measurements of the L-PBF 2205 DSS as-built and after different annealing treatments. The cold-rolled 2205 alloy microhardness value is included for comparison. The table is adapted from [43]. The data are presented as mean value ± standard deviation.

Sample	As Built	Annealed 950/5	Annealed 1000/5	Annealed 1050/5	Annealed 1100/5	Annealed 1000/60	Annealed 1050/60	Cold-Rolled 2205 DSS
Hardness (HV)	336.6 ± 6.4	279.9 ± 10.3	279.8 ± 11.2	270.5 ± 8.8	255.2 ± 4.2	262.6 ± 9.6	265.0 ± 8.5	247.0 ± 1.5

Hongliang Xiang et al. [44] investigated the effect of different solution temperatures (1000 °C, 1100 °C, and 1200 °C) on the evolution of the phase and microstructure, and consequently on the mechanical properties of L-PBF Fe-22Cr-5Ni-0.26N DSS. The results, in terms of microhardness values, revealed that the hardness of the as built L-PBF sample reached the highest HV value. After the solution treatment, the hardness declined by raising the temperature, even if the HV values were all higher than those of the forged samples (Figure 19) [44].

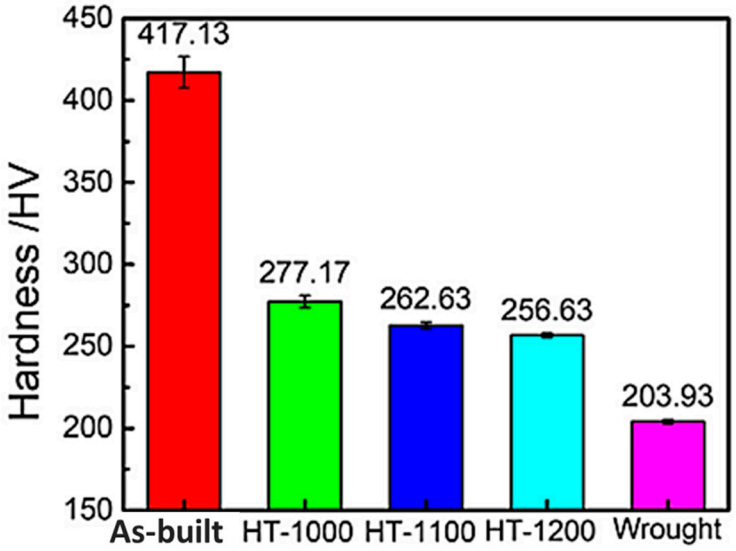


Figure 19. Hardness measurements of as-built, solution-treated, and forged samples. The figure is adapted from [44]. The online version of this article should be consulted for an explanation of the colour references in this graphic.

3.3.2. Tensile Properties

DSS typically has 1.5 times the tensile strength of austenitic SS [62]. The presence of two phases hinders the growth of grains, whose size in austenitic SS can be significantly larger than in DSS. This explains why DSS has higher strength and ductility than austenitic SS. Due to the solution strengthening effect, the addition of alloying elements may also boost the material's strength [8,63]. Raising the percentage of ferrite enhances the material's strength, but reduces its ductility and toughness. The FCC structure of austenite allows for greater plastic deformation tolerance and enhances the ductility of the duplex stainless steel [64]. As a result of fine grains, excessive ferrite phase, nitride precipitation, and high dislocation density, DSS samples produced by L-PBF have the highest tensile strength compared to their wrought counterparts, at over 900 MPa, but the lowest elongation, which is often at about 10% [52]. The precipitation of the σ phase degrades the ductility significantly [58]. Suvi Papula et al. [43] showed the results of tensile tests conducted on DSS 2205 specimens produced by L-PBF, compared with typical values of tensile properties of the conventionally cold-rolled and annealed alloy (Table 5) [43]. The yield strength (520–560 MPa) and tensile strength (810–870 MPa) of the L-PBF-processed and heat-treated specimens were significantly greater than those of the conventionally-produced alloy with

a similar chemical composition, but the uniform elongation was within a comparable range (23–25%) [43].

Table 5. The tensile mechanical properties of as-built, heat-treated, and forged DSS. The table was adapted from [43]. The data are presented as mean value ± standard deviation.

Sample	As-Built	Annealed 950°/5	Annealed 1000°/5	Annealed 1050°/5	Annealed 1100°/5	Annealed 1000°/60	Annealed 1050°/60	Ref. Alloy 2205
Yield strength (MPa)	950.0 ± 9.2	560.8 ± 3.3	549.0 ± 4.9	535.5 ± 9.2	524.0 ± 2.8	531.7 ± 2.5	517.1 ± 2.9	450–500
Tensile strength (MPa)	1071.3 ± 6.9	868.7 ± 2.3	848.0 ± 1.0	836.7 ± 1.1	813.0 ± 0.6	824.4 ± 1.8	812.1 ± 4.1	600–655
Uniform elongation (%)	7.0 ± 1.3	22.9 ± 0.4	23.9 ± 1.2	24.4 ± 1.1	24.1 ± 0.4	25.2 ± 0.9	25.3 ± 0.9	>25
Elongation to fracture (%)	16.0 ± 1.1	39.7 ± 1.6	45.8 ± 2.6	42.1 ± 3.5	39.7 ± 3.4	43.4 ± 2.5	41.8 ± 1.5	–

Hongliang Xiang et al. [44] examined the effects of three solution temperatures (1000 °C, 1100 °C, and 1200 °C) on the evolution of the phase and microstructure of Fe22Cre5Ni-0.26N DSS manufactured by L-PBF in order to obtain exceptional strength-plasticity matching. The outcomes were then utilized to explain the associated changes in the mechanical characteristics of the specimens under tensile stress. According to the results, the as-built specimen exhibited the highest ultimate tensile strength, yield strength, and low elongation (Figure 20A). Due to the recovery of two-phase structures, the refining of grains, and the elimination of dislocations and residual stresses through recrystallization, the specimen subjected to a solution treatment at a temperature of 1000 °C exhibited a remarkable strength-plasticity match and a significant increase in elongation. When the temperature increased, the yield strength decreased, but elongation remained almost unchanged. Figure 20B–D [44] illustrates that, with the exception of elongation, the tensile and yield strengths of L-PBF specimens were greater than those of the forged specimens.

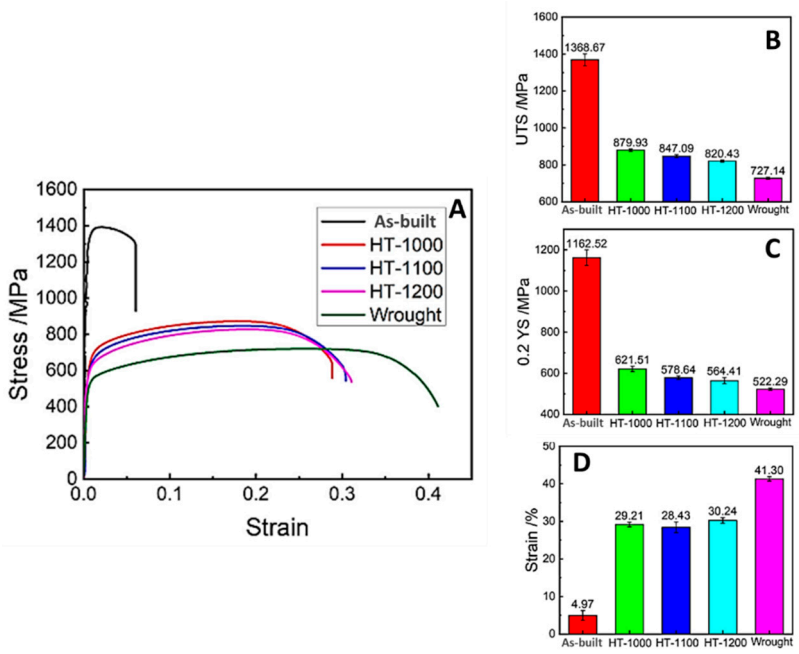


Figure 20. Mechanical tensile test of L-PBF Fe22Cre5Ni-0.26N DSS: (**A**) Stress-strain curves of the specimens; and (**B**–**D**) Experimental values of ultimate tensile strength (UTS), yield strength at 0.2% of strain (0.2% YS), and strain, respectively. The figures were adapted from [44]. The online version of this article should be consulted for an explanation of the colour references in this graphic.

Hengsbach et al. [47] conducted a mechanical characterization of UNS S31803 (2205 alloy) processed by L-PB,F on as-built and heat-treated specimens, revealing that the almost fully ferritic as-built specimens have a higher ultimate tensile strength and less elongation at fracture then the heat-treated samples (Figure 21). As a result of the recrystallized austenitic-ferritic microstructure, the mechanical properties of the heat-treated samples contrast with those of the as-built state, as they exhibit a high degree of ductility (Figure 21) due to the reduced dislocation density and the dissolution of Cr2N, in addition to the phase change.

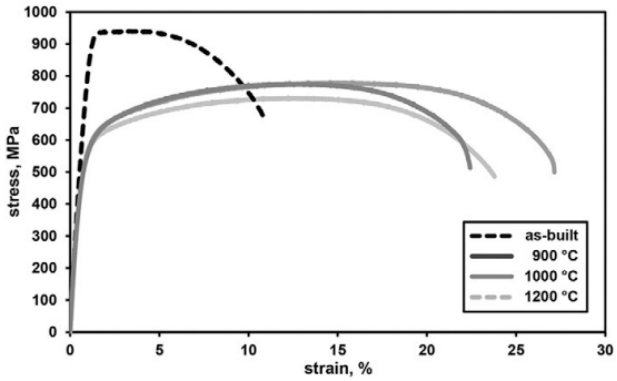


Figure 21. Tensile stress-strain curves for S31803 DSS (2205 alloy) produced by L-PBF in the as-built and annealed conditions. The figure was adapted with permission from [47]. Copyright (2017), Elsevier.

In terms of high ultimate strength and low ductility, Saedi et al. [52] obtained identical outcomes for a super DSS in its as-built state. This material's behavior can be related to the high dislocation density and the presence of nitrides, which inhibit dislocation movement and, as a result, strengthen the material. Following annealing, the fully recrystallized specimens attain a tensile strength of between 720 and 770 MPa. Considering elongation at fracture, annealing at 1000 °C is the most advantageous heat treatment, exhibiting approximately 28% elongation; this condition also displays the largest austenite volume fraction. Additionally, differing annealing temperatures have a significant effect on the elongation at fracture. At lower annealing temperatures, it is believed that sigma-phase and nitride precipitation are primarily responsible for the reduced elongation at fracture. In addition, there is less austenite found in the 900 °C condition. At higher annealing temperatures, such as 1200 °C, the mainly lower proportion of austenite content causes a decrease in fracture elongation. This analysis revealed that the condition with the highest austenite content had the most desired mechanical characteristics [47]. Nigon et al. [42] investigated the effect of annealing on the L-PBF 2205 DSS. The as-built samples were hard and brittle. The heat treatment restored ductility, although the material's characteristics were still inferior to the wrought sample, as reported in Table 6.

Table 6. The outcomes of mechanical property tests on DSS 2205 fabricated by L-PBF at 187 W and 800 mm/s [42].

Sample	Yield Strength (MPa)	Tensile Strength (MPa)	Elongation (%)
As-built	826 ± 32	872 ± 33	11 ± 2
Heat treated	465 ± 3	622 ± 19	21.3 ± 1.4
Wrought (ASTM A790)	655 (448)	882 (621–1103)	25 (25)

The mechanical properties of the DSS component produced by L-PBF, such as microhardness, tensile yield, tensile strength, and elongation, were significantly influenced by the ratio of ferrite/austenite, the precipitation of secondary brittle phases, the formation

of nitrides, and grain size. The as-built samples typically show the highest values of mechanical properties (i.e., tensile) and microhardness. On the other hand, heat treatments are useful in improving the elongation of the as-built samples, although the final values are still lower than for that of the wrought counterpart. For the sake of comparison, a comprehensive summary of the mechanical properties of DSS fabricated by L-PBF from the literature is reported in Table 7, together with the experimental results of the same DSS alloy produced by forging.

Table 7. A summary of the mechanical properties of DSS fabricated by the L-PBF technique collected from the literature. The experimental results of the same DSS alloys produced by forging are reported for the sake of comparison.

DSS	Reference	VED (J/mm^3)	Sample	Hardness (HV)	Yield Strength (MPa)	Tensile Strength (MPa)	Elongation (%)
2205	[47]	59	as built HT 900 °C HT 1000 °C HT 1200 °C	–	–	940 720 ÷ 760	12 28 (HT 1000 °C)
2205	[42]	156	wrought as built HT 1100 °C	267 419 258	655 826 465	882 872 622	25 11 21.3
2507	[52]	127	as built	450	1214	1321	>45
2507	[41]	91.7–141	as built	408.4 (91.7 J/mm^3)	–	–	–
2507	[26]	84.6–112.8	as built	447.8 (VED = 49.4 J/mm^3) ÷ decreasing	–	–	–
2507	[60]	133	HT 1200 °C	400	686	920	1.8
2205	[43]	–	ref. 2205 (from DSS producer) as built HT 950 °C/5 min HT 1000 °C/5 min HT 1050 °C/5 min HT 1100 °C/5 min	–	450 ÷ 500 950 560.8 549 535.5 524	600 ÷ 655 1071.3 868.7 848 836.7 813	>25 7 22.9 23.9 24.4 24.1
Fe-22Cr-5Ni-0.26N	[44]	79	wrought as built HT 1000 °C HT 1100 °C HT 1200 °C	203.93 417.13 277.17 262.63 256.63	522.29 1162.52 621.51 578.64 564.41	727.14 1368.67 879.93 847.09 820.43	41.30 4.97 29.21 28.43 30.24

3.3.3. Fatigue Behaviour

General speaking, the mechanical properties, especially fatigue strength, of the final component are negatively influenced by surface roughness and the formation of defects such as residual porosity and the lack of fusion, which act as stress concentration areas [65,66]. Kunz et al. [67] investigated the effect of hot isostatic pressing (HIP) post-treatment on the fatigue behavior of standard DSS 2205 and super DSS 2207 fabricated by LPBF. Compared to sand-cast samples, the fatigue strength of as-built DSS 2205 was significantly lower at 203 MPa than at 367 MPa. Due to the attachment of powder particles, the formation of a porosity defect, and the anisotropic microstructure, the lower fatigue strength can be explained by the high surface roughness. In addition, the austenite phase exhibited a greater plastic deformation capacity than ferrite, thereby absorbing energy and reducing notch sensitivity. The microstructure of the LPBF specimens was entirely ferritic, resulting in a high resistance to notch sensitivity. In order to enhance the fatigue properties of LPBF samples, surface modification, post-heat treatment, and HIP were employed. The solution treatment increased the fatigue strength from 203 to 372 MPa by eliminating the predominant ferritic structure. The solution treatment enhanced the fatigue strength from

203 MPa to 372 MPa through the elimination of the predominant ferritic structure. Due to the considerable reduction in porosity brought about by HIP, the fatigue strength was raised to 470 MPa [67].

3.4. Corrosion Resistance

The corrosion resistance of AM DSS is typically equivalent to or lower than that of traditionally fabricated counterparts, and the as-built condition is vulnerable to pitting in comparison to the annealed condition [8,43]. The corrosion resistance of DSS was degraded by the loss of alloy elements, porosity, surface roughness, residual tensile stress, secondary phases (particularly the σ phase), and an imbalanced two-phase ratio during additive manufacturing. Post-heat treatment, surface modification, and HIP can be used to efficiently recover DSS's resistance to pitting. However, it is worth noting that the relationship between the corrosion resistance of DSS produced by L-PBF and the microstructure properties is still being considered by the scientific community [8,68].

Nigon et al. [42] analyzed the influence of building orientation and heat treatment on the corrosion resistance of L-PBF 2205 DSS. There was no stable pit development; however, metastable pitting was detected on all samples, with the exception of the as-built parallel samples. The remaining porosity and/or chemical inhomogeneity were likely responsible for the metastable pitting. Despite significant textural and microstructural changes across samples at different building orientations and heat treatments, the evaluated pitting corrosion resistance was similar for all of the L-PBF samples, and was comparable to the DSS 2205 wrought samples. This suggests that the bulk chemical composition was the dominant element with regard to pitting corrosion resistance [42]. Suvi Papula et al. [43] focused their investigation on L-PBF of DSS 2205 in its as-built condition, and after undergoing several post-processing heat treatments. Figure 22 illustrates the corrosion test results. The marked hysteresis was found when the polarization direction was reversed, and the return polarization curve followed an active path. Owing to material porosity, the re-passivation potential of as-built L-PBF DSS was lowered (Figure 22). The pitting corrosion resistance of L-PBF samples rose substantially as a result of successive heat treatments. In chloride-rich environments, the corrosion resistance of DSS exceeds that of ferritic and austenitic single-phase SS [43].

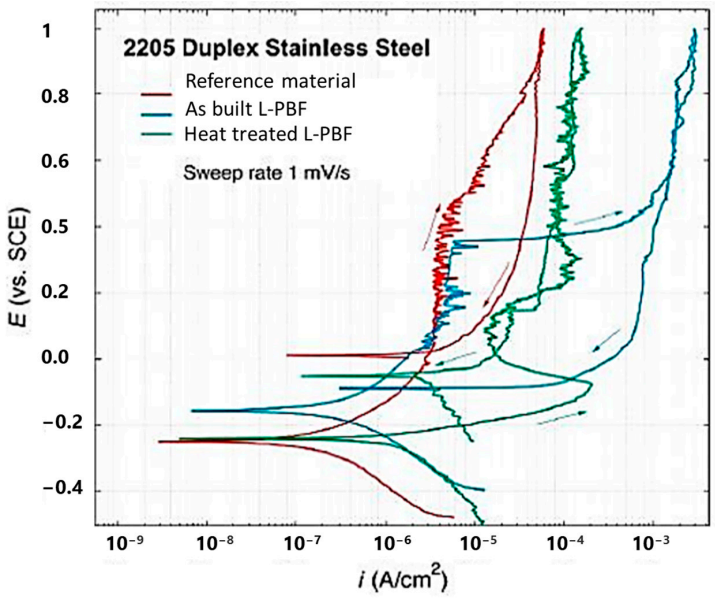


Figure 22. Cyclic potentiodynamic polarization curves of L-PBF 2205 DSS in as-built, cold-rolled and annealed conditions, using a neutral 0.6 M NaCl solution as a post-heat treatment at room temperature. The direction of polarization is represented by the arrows. The figure is adapted from [43].

In addition to the standard 2205 DSS, the corrosion resistance of super DSS fabricated by L-PBF is extensively documented. Murkute et al. [48] determined that when the scan speed increased from 100 to 1000 mm/s, the corrosion resistance of the deposited super DSS 2507 layers decreased. A low scan speed (100 mm/s) exhibited a corrosion resistance similar to that of rolled and annealed super DSS [48]. The corrosion rates of the solution-treated samples were much lower than those of the as-built samples. For as-built samples, the residual tensile stress led to a high corrosion rate. The residual stress was removed, and the corrosion resistance was restored by heat treatment [48]. Shang et al. [69] discovered that the correct solution treatment raised the content of austenite from 0.2% to 40.5% and significantly enhanced the pitting corrosion resistance [69]. Jiang et al. [70] also evaluated the effect of chemical compositions and solution treatment on the corrosion resistance of L-PBF samples. The findings of cyclic potentiodynamic polarization demonstrated that, at room temperature, both as-built and solution-treated samples exhibited the same response as their wrought counterparts. [70]. The optimal ferrite to austenite ratio for DSS corrosion resistance is approximately 1 [43].

3.5. Magnetic Properties

The high ferrite fraction of AM-produced DSS leads to markedly different magnetic properties of L-PBF samples from the conventionally produced ones. The saturation magnetization and the coercivity in 2507 DSS processed with L-PBF are both much higher than in its conventionally produced counterpart, apart from anisotropic hysteresis results [26]. In particular, the average saturation magnetism (Ms) of L-PBF DSS is around 110 Am^2 /kg, which is more than double the maximum saturation level achievable with the corresponding wrought material (Figure 23A). L-PBF samples display robust soft magnetic properties with an average coercivity (Hc) of 1.81 mT (Figure 23B). The grain anisotropy of L-PBF DSS results in directional specific saturation magnetism and coercivity responses [26]. In addition, the AM-typical strong fibre texture induces a significant anisotropy in the soft magnetic characteristics [53].

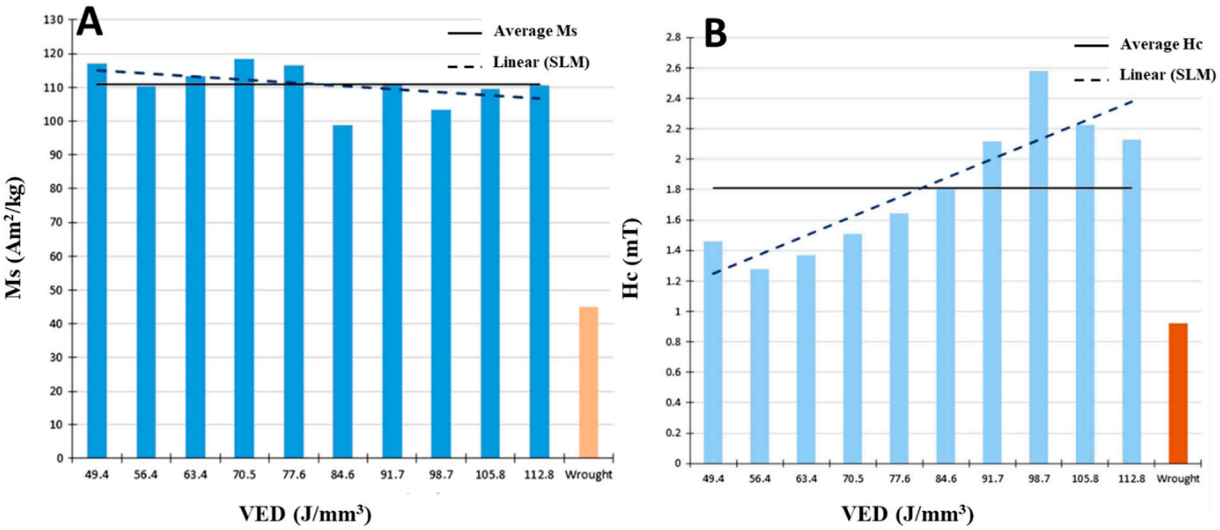


Figure 23. Magnetic properties of 2507 DSS processed by L-PBF samples: (**A**) Saturation magnetism results; and (**B**) Coercivity results. Ms-saturation magnetism; Hc-coercivity. Figures adapted with permission from [26]. Copyright (2016), Springer Nature.

4. Conclusions

The present paper addressed the topic of duplex stainless steels (DSS) processed by laser powder bed fusion (L-PBF) additive manufacturing technology. This process enables the fabrication of complex geometries and highly customized parts (i.e., patient-specific devices) with fine details. These peculiarities make L-PBF the most suitable metal AM

technology for biomedical applications. DSS has been considered as a good candidate for these applications in the past, with a slow but relentless decrease from year to year of its inclusion in trials and experimental studies for the fabrication of medical devices. The reason for this decline has to be found in the fact that fabrication technologies have a remarkable impact on defining the final properties of any alloy, and this is also true for DSS, whose magnetic and corrosion behavior (in particular) are determined by the microstructure and phase composition. With the development and optimization of advanced processing technologies based on a layer-upon-layer fabrication and characterized by solidification rates as high as 10^6 K/s, the results reported in the present paper highlight that a new era of duplex stainless steels produced by L-PBF technology has already begun. The literature shows that by tuning the process parameters and the post-processing heat treatments, it is possible not only to control the final microstructure, but to tailor the behaviour of the DSS for the final application, enhancing its already-assessed potential as a metallic material for biomedical applications.

The main conclusions based on literature can be listed as follows:

- Residual porosity and lack of fusion of the L-PBF processed duplex stainless steels (DSS) are controlled by the volumetric energy density (VED), in order to obtain full dense components;
- The arrangement of the austenite-ferrite phases is balanced upon the subsequent heat-treatment of as-built samples;
- The hardness and tensile strength of L-PBF DSS exceeds that of conventionally produced steels, also showing superior corrosion and magnetic properties.

This review work evidenced the suitability of laser powder bed fusion technology for producing duplex stainless steel temporary implants for bone tissue regeneration. Processing parameter optimization and post-production heat treatments allow for the designing of the microstructure and for controlling the defects of the fabricated DSS, improving its mechanical properties, corrosion resistance, and magnetic behaviour with respect to the DSS performances obtained using conventional production techniques. Moreover, L-PBF geometric freedom and high dimensional accuracy introduce very important perspectives in the fields of patient customized DSS implants for bone regeneration and tissue engineering.

Author Contributions: M.L.G.: Conceptualization, investigation, writing—original draft; A.S.: Conceptualization, investigation, writing—original draft; E.S.: Conceptualization, visualization, writing—original draft; S.S.: Methodology, validation, formal analysis; F.F.: Methodology, writing—review and editing, data curation; P.M.: Supervision, writing—review and editing, validation; M.C.: Supervision, data curation, validation. All authors have read and agreed to the published version of the manuscript.

Funding: This research was partially funded by the Grant of Excellence Departments, MIUR-Italy (ARTICOLO 1, COMMI 314–337 LEGGE 232/2016).

Data Availability Statement: Data sharing is not applicable to this article.

Conflicts of Interest: The authors declare no conflict of interest.

References

1. López, D.A.; Durán, A.; Ceré, S. Electrochemical characterization of AISI 316L stainless steel in contact with simulated body fluid under infection conditions. *J. Mater. Sci. Mater. Med.* **2008**, *19*, 2137–2144. [CrossRef] [PubMed]
2. Chakraborty Banerjee, P.; Al-Saadi, S.; Choudhary, L.; Harandi, S.E.; Singh, R. Magnesium implants: Prospects and challenges. *Materials* **2019**, *12*, 136. [CrossRef]
3. Roman, A.M.; Geantă, V.; Cimpoeșu, R.; Munteanu, C.; Lohan, N.M.; Zegan, G.; Cernei, E.R.; Ionită, I.; Cimpoes, N.; Ioanid, N. In-vitro analysis of FeMn-Si smart biodegradable alloy. *Materials* **2022**, *15*, 568. [CrossRef] [PubMed]
4. Bekmurzayeva, A.; Duncanson, W.J.; Azevedo, H.S.; Kanayeva, D. Surface modification of stainless steel for biomedical applications: Revisiting a century-old material. *Mater. Sci. Eng. C* **2018**, *93*, 1073–1089. [CrossRef] [PubMed]
5. Gregorutti, R.W.; Grau, J.E.; Sives, F.; Elsner, C.I. Mechanical, electrochemical and magnetic behaviour of duplex stainless steel for biomedical applications. *Mater. Sci. Technol.* **2015**, *31*, 1818–1824. [CrossRef]

6. Cigada, A.; Rondelli, G.; Vicentini, B.; Giacomazzi, M.; Roos, A. Duplex stainless steels for osteosynthesis devices. *J. Biomed. Mater. Res.* **1989**, *23*, 1087–1095. [CrossRef]
7. Hammood, A.S. Biomineralization of 2304 duplex stainless steel with surface modification by electrophoretic deposition. *J. Appl. Biomater. Funct. Mater.* **2020**, *18*, 2280800019896215. [CrossRef] [PubMed]
8. Zhang, D.; Liu, A.; Yin, B.; Wen, P. Additive manufacturing of duplex stainless steels-a critical review. *J. Manuf. Process.* **2022**, *73*, 496–517. [CrossRef]
9. Han, Y.; Liu, Z.H.; Wu, C.B.; Zhao, Y.; Zu, G.Q.; Zhu, W.W.; Ran, X. A short review on the role of alloying elements in duplex stainless steels. *Tungsten* **2022**, 1–21. [CrossRef]
10. Kain, V. Stress corrosion cracking (SCC) in stainless steels. In *Stress Corrosion Cracking*; Woodhead Publishing: Sawston, Cambridge, UK, 2011; pp. 199–244. [CrossRef]
11. Charles, J. Duplex families and applications: A review. Part 1: From duplex pioneers up to 1991. In *Stainless SteelWorld*; KCI Group: Sparks, MD, USA, 2015; pp. 1–5.
12. Freitas, G.C.L.D.; da Fonseca, G.S.; Moreira, L.P.; Leite, D.N.F. Phase transformations of the duplex stainless steel UNS S31803 under non-isothermal conditions. *J. Mater. Res. Technol.* **2021**, *11*, 1847–1851. [CrossRef]
13. Fonseca, G.S.D.; Mendes, P.S.N.; Silva, A.C.M. Sigma phase: Nucleation and growth. *Metals* **2019**, *9*, 34. [CrossRef]
14. Biezma, M.V.; Martin, U.; Linhardt, P.; Ress, J.; Rodríguez, C.; Bastidas, D.M. Non-destructive techniques for the detection of sigma phase in duplex stainless steel: A comprehensive review. *Eng. Fail. Anal.* **2021**, *122*, 105227. [CrossRef]
15. Mahajan, A.; Sidhu, S.S.; Devgan, S. Examination of hemocompatibility and corrosion resistance of electrical discharge-treated duplex stainless steel (DSS-2205) for biomedical applications. *Appl. Phys. A* **2020**, *126*, 737. [CrossRef]
16. Hammood, A.S.; Naser, M.S.; Radeef, Z.S. Electrophoretic Deposition of Nanocomposite Hydroxyapatite/Titania Coating on 2205 Duplex Stainless Steel Substrate. *Jom* **2021**, *73*, 524–533. [CrossRef]
17. Hammood, A.S.; Noor, A.F.; Alkhafagy, M.T. Evaluation of corrosion behavior in artificial saliva of 2507 and 2205 duplex stainless steel for orthodontic wires before and after heat treatment. *J. Mater. Sci. Mater. Med.* **2017**, *28*, 187. [CrossRef] [PubMed]
18. Kumar, R.; Kumar, M.; Chohan, J.S. The role of additive manufacturing for biomedical applications: A critical review. *J. Manuf. Process.* **2021**, *64*, 828–850. [CrossRef]
19. Cook, D.; Gervasi, V.; Rizza, R.; Kamara, S.; Liu, X.C. Additive fabrication of custom pedorthoses for clubfoot correction. *Rapid Prototyp. J.* **2010**, *16*, 189–193. [CrossRef]
20. Han, C.; Fang, Q.; Shi, Y.; Tor, S.B.; Chua, C.K.; Zhou, K. Recent advances on high-entropy alloys for 3D printing. *Adv. Mater.* **2020**, *32*, 1903855. [CrossRef]
21. Wang, D.; Liu, L.; Deng, G.; Deng, C.; Bai, Y.; Yang, Y.; Wu, W.; Chen, J.; Liu, Y.; Wang, Y.; et al. Recent progress on additive manufacturing of multi-material structures with laser powder bed fusion. *Virtual Phys. Prototyp.* **2022**, *17*, 329–365. [CrossRef]
22. Singh, R.; Gupta, A.; Tripathi, O.; Srivastava, S.; Singh, B.; Awasthi, A.; Rajput, S.K.; Sonia, P.; Singhal, P.; Saxena, K.K. Powder bed fusion process in additive manufacturing: An overview. *Mater. Today Proc.* **2020**, *26*, 3058–3070. [CrossRef]
23. Yang, N.; Gong, Y.; Chen, H.; Li, W.; Zhou, C.; Zhou, R.; Shao, H. Personalized Artificial Tibia Bone Structure Design and Processing Based on Laser Powder Bed Fusion. *Machines* **2022**, *10*, 205. [CrossRef]
24. Munsch, M. Laser additive manufacturing of customized prosthetics and implants for biomedical applications. In *Laser Additive Manufacturing*; Woodhead Publishing: Sawston, Cambridge, UK, 2017; pp. 399–420. [CrossRef]
25. Sing, S.L.; An, J.; Yeong, W.Y.; Wiria, F.E. Laser and electron-beam powder-bed additive manufacturing of metallic implants: A review on processes, materials and designs. *J. Orthop. Res.* **2016**, *34*, 369–385. [CrossRef] [PubMed]
26. Davidson, K.P.; Singamneni, S. Magnetic characterization of selective laser-melted Saf 2507 duplex stainless steel. *Jom* **2017**, *69*, 569–574. [CrossRef]
27. Sathiyanarayanan, S.; Marikkannu, C.; Srinivasan, P.B.; Muthupandi, V. Corrosion behaviour of Ti6Al4V and duplex stainless steel (UNS31803) in synthetic bio-fluids. *Anti-Corrosion Methods Mater.* **2002**, *49*, 33–37. [CrossRef]
28. Cigada, A.; Amici, F.; Cavallini, M.; De Santis, G.; Gatti, A.M.; Giacomazzi, M.; Rondelli, G.; Roos, A.; Vicentini, B.; Zaffe, D. Characterization of a high performance duplex stainless steel for orthopedic applications. In Proceedings of the Twelfth Annual International Conference of the IEEE Engineering in Medicine and Biology Society, Philadelphia, PA, USA, 1–4 November 1990; pp. 2082–2084. [CrossRef]
29. Barbosa, M.A. *Chapter 10 Corrosion of Metallic Implants. Handbook of biomaterial properties*; Springer: New York, NY, USA, 2016; pp. 509–548.
30. Pan, J.; Karlen, C.; Ulfvin, C. Electrochemical study of resistance to localized corrosion of stainless steels for biomaterial applications. *J. Electrochem. Soc.* **2000**, *147*, 1021. [CrossRef]
31. Köse, C. Characterization of weld seam surface and corrosion behavior of laser-beam-welded AISI 2205 duplex stainless steel in simulated body fluid. *J. Mater. Sci.* **2020**, *55*, 17232–17254. [CrossRef]
32. Platt, J.A.; Guzman, A.; Zuccari, A.; Thornburg, D.W.; Rhodes, B.F.; Oshida, Y.; Moore, B.K. Corrosion behavior of 2205 duplex stainless steel. *Am. J. Orthod. Dentofac. Orthop.* **1997**, *112*, 69–79. [CrossRef]
33. Cigada, A.L.B.E.R.T.O.; Santis, G.D.; Gatti, A.M.; Roos, A.; Zaffe, D. In vivo behavior of a high performance duplex stainless steel. *J. Appl. Biomater.* **1993**, *4*, 39–46. [CrossRef]
34. Park, B.H.; Koo, B.S.; Kim, Y.K.; Kim, M.K. The induction of hyperthermia in rabbit liver by means of duplex stainless steel thermoseeds. *Korean J. Radiol.* **2022**, *3*, 98–104. [CrossRef]

35. DebRoy, T.; Wei, H.L.; Zuback, J.S.; Mukherjee, T.; Elmer, J.W.; Milewski, J.O.; Zhang, W. Additive manufacturing of metallic components–process, structure and properties. *Prog. Mater. Sci.* **2018**, *92*, 112–224. [CrossRef]
36. Davidson, K.; Singamneni, S. Selective laser melting of duplex stainless steel powders: An investigation. *Mater. Manuf. Process.* **2016**, *31*, 1543–1555. [CrossRef]
37. Bertoli, U.S.; Wolfer, A.J.; Matthews, M.J.; Delplanque, J.P.R.; Schoenung, J.M. On the limitations of volumetric energy density as a design parameter for selective laser melting. *Mater. Des.* **2017**, *113*, 331–340. [CrossRef]
38. Zhao, C.; Parab, N.D.; Li, X.; Fezzaa, K.; Tan, W.; Rollett, A.D.; Sun, T. Critical instability at moving keyhole tip generates porosity in laser melting. *Science* **2020**, *370*, 1080–1086. [CrossRef]
39. du Plessis, A. Effects of process parameters on porosity in laser powder bed fusion revealed by X-ray tomography. *Addit. Manuf.* **2019**, *30*, 100871. [CrossRef]
40. Knezović, N.; Garašić, I.; Jurić, I. Influence of the interlayer temperature on structure and properties of wire and arc additive manufactured duplex stainless steel product. *Materials* **2020**, *13*, 5795. [CrossRef] [PubMed]
41. Davidson, K.P.; Singamneni, S.B. Metallographic evaluation of duplex stainless steel powders processed by selective laser melting. *Rapid Prototyp. J.* **2017**, *23*, 1146–1163. [CrossRef]
42. Nigon, G.N.; Isgor, O.B.; Pasebani, S. The effect of annealing on the selective laser melting of 2205 duplex stainless steel: Microstructure, grain orientation, and manufacturing challenges. *Opt. Laser Technol.* **2021**, *134*, 106643. [CrossRef]
43. Papula, S.; Song, M.; Pateras, A.; Chen, X.B.; Brandt, M.; Easton, M.; Hänninen, H. Selective laser melting of duplex stainless steel 2205: Effect of post-processing heat treatment on microstructure, mechanical properties, and corrosion resistance. *Materials* **2019**, *12*, 2468. [CrossRef]
44. Xiang, H.; Zhao, W.; Lu, Y. Effect of solution temperature on microstructure and mechanical properties of selective laser melted Fe–22Cr–5Ni-0.26 N duplex stainless steel. *J. Mater. Res. Technol.* **2022**, *19*, 1379–1389. [CrossRef]
45. Bartlett, A.A. Demonstration of a crystalline phase change in a solid. *Phys. Teach.* **1975**, *13*, 545–547. [CrossRef]
46. Arumugham Akilan, A.; Enneti, R.K.; Balla, V.K.; Atre, S.V. Effects of Hot Isostatic Pressing on the Properties of Laser-Powder Bed Fusion Fabricated Water Atomized 25Cr7Ni Stainless Steel. *Lubricants* **2022**, *10*, 340. [CrossRef]
47. Hengsbach, F.; Koppa, P.; Duschik, K.; Holzweissig, M.J.; Burns, M.; Nellesen, J.; Schaper, M. Duplex stainless steel fabricated by selective laser melting-Microstructural and mechanical properties. *Mater. Des.* **2017**, *133*, 136–142. [CrossRef]
48. Murkute, P.; Pasebani, S.; Burkan Isgor, O. Metallurgical and electrochemical properties of super duplex stainless steel clads on low carbon steel substrate produced with laser powder bed fusion. *Sci. Rep.* **2020**, *10*, 10162. [CrossRef] [PubMed]
49. Li, H.B.; Jiang, Z.H.; Zhang, Z.R.; Yang, Y. Effect of grain size on mechanical properties of nickel-free high nitrogen austenitic stainless steel. *J. Iron Steel Res. Int.* **2009**, *16*, 58–61. [CrossRef]
50. Mukherjee, T.; DebRoy, T. A digital twin for rapid qualification of 3D printed metallic components. *Appl. Mater. Today* **2019**, *14*, 59–65. [CrossRef]
51. Wei, H.L.; Mukherjee, T.; Zhang, W.; Zuback, J.S.; Knapp, G.L.; De, A.; DebRoy, T. Mechanistic models for additive manufacturing of metallic components. *Prog. Mater. Sci.* **2021**, *116*, 100703. [CrossRef]
52. Saeidi, K.; Kevetkova, L.; Lofaj, F.; Shen, Z. Novel ferritic stainless steel formed by laser melting from duplex stainless steel powder with advanced mechanical properties and high ductility. *Mater. Sci. Eng. A* **2016**, *665*, 59–65. [CrossRef]
53. Bajaj, P.; Hariharan, A.; Kini, A.; Kürnsteiner, P.; Raabe, D.; Jägle, E.A. Steels in additive manufacturing: A review of their microstructure and properties. *Mater. Sci. Eng. A* **2020**, *772*, 138633. [CrossRef]
54. Mahale, R.S.; Rajendrachari, S.; Vasanth, S.; Krishna, H.; Kapanigowda, N.S.; Chikkegowda, S.P.; Patil, A. Technology and challenges in additive manufacturing of duplex stainless steels. *Biointerface Res. Appl. Chem.* **2022**, *12*, 1110–1119. [CrossRef]
55. Chan, K.W.; Tjong, S.C. Effect of secondary phase precipitation on the corrosion behavior of duplex stainless steels. *Materials* **2014**, *7*, 5268–5304. [CrossRef]
56. Deng, B.; Wang, Z.; Jiang, Y.; Sun, T.; Xu, J.; Li, J. Effect of thermal cycles on the corrosion and mechanical properties of UNS S31803 duplex stainless steel. *Corros. Sci.* **2009**, *51*, 2969–2975. [CrossRef]
57. Verma, J.; Taiwade, R.V. Effect of welding processes and conditions on the microstructure, mechanical properties and corrosion resistance of duplex stainless steel weldments—A review. *J. Manuf. Process.* **2017**, *25*, 134–152. [CrossRef]
58. Atamert, S.; King, J.E. Sigma-phase formation and its prevention in duplex stainless steels. *J. Mater. Sci. Lett.* **1993**, *12*, 1144–1147. [CrossRef]
59. Kokawa, H.; Tomita, M.; Kuwana, T. Effect of nitrogen on impact toughness of duplex stainless steel weld metal. *Weld. Int.* **1995**, *9*, 217–224. [CrossRef]
60. Saeidi, K.; Alvi, S.; Lofaj, F.; Petkov, V.I.; Akhtar, F. Advanced mechanical strength in post heat treated SLM 2507 at room and high temperature promoted by hard/ductile sigma precipitates. *Metals* **2019**, *9*, 199. [CrossRef]
61. Souza, E.C.D.; Rossitti, S.M.; Fortulan, C.A.; Rollo, J.M.D.D.A. Influence of ferrite phase content on the electrochemical properties of duplex stainless steels. *Mater. Res.* **2016**, *20*, 21–29. [CrossRef]
62. Hwang, H.; Park, Y. Effects of heat treatment on the phase ratio and corrosion resistance of duplex stainless steel. *Mater. Trans.* **2009**, *50*, 1548–1552. [CrossRef]
63. Badji, R.; Bouabdallah, M.; Bacroix, B.; Kahloun, C.; Belkessa, B.; Maza, H. Phase transformation and mechanical behavior in annealed 2205 duplex stainless steel welds. *Mater. Charact.* **2008**, *59*, 447–453. [CrossRef]

64. Yilmaz, H.; Williams, C.J.; Derby, B. Size effects on strength and plasticity of ferrite and austenite pillars in a duplex stainless steel. *Mater. Sci. Eng. A* **2020**, *793*, 139883. [CrossRef]
65. Fischer, T.; Kuhn, B.; Rieck, D.; Schulz, A.; Trieglaff, R.; Wilms, M.B. Fatigue Cracking of Additively Manufactured Materials—Process and Material Perspectives. *Appl. Sci.* **2020**, *10*, 5556. [CrossRef]
66. Molaei, R.; Fatemi, A. Fatigue design with additive manufactured metals: Issues to consider and perspective for future research. *Procedia Eng.* **2018**, *213*, 5–16. [CrossRef]
67. Kunz, J.; Boontanom, A.; Herzog, S.; Suwanpinij, P.; Kaletsch, A.; Broeckmann, C. Influence of hot isostatic pressing post-treatment on the microstructure and mechanical behavior of standard and super duplex stainless steel produced by laser powder bed fusion. *Mater. Sci. Eng. A* **2020**, *794*, 139806. [CrossRef]
68. Soleimani, M.; Mirzadeh, H.; Dehghanian, C. Effect of grain size on the corrosion resistance of low carbon steel. *Mater. Res. Express* **2020**, *7*, 016522. [CrossRef]
69. Shang, F.; Chen, X.; Wang, Z.; Ji, Z.; Ming, F.; Ren, S.; Qu, X. The microstructure, mechanical properties, and corrosion resistance of UNS S32707 hyper-duplex stainless steel processed by selective laser melting. *Metals* **2019**, *9*, 1012. [CrossRef]
70. Jiang, D.; Birbilis, N.; Hutchinson, C.R.; Brameld, M. On the microstructure and electrochemical properties of additively manufactured duplex stainless steels produced using laser-powder bed fusion. *Corrosion* **2020**, *76*, 871–883. [CrossRef]

Disclaimer/Publisher's Note: The statements, opinions and data contained in all publications are solely those of the individual author(s) and contributor(s) and not of MDPI and/or the editor(s). MDPI and/or the editor(s) disclaim responsibility for any injury to people or property resulting from any ideas, methods, instructions or products referred to in the content.